Springer

Acta Mechanica Sinica

CrossMark click for updates

• RESEARCH PAPER •

Acta Mech. Sin., Vol. 41, 424095 (2025)
https://doi.org/10.1007/s10409-024-24095-x

Characterization of elastic modulus and hardness of brittle solids by instrumented indentation

Zhitong Xu[1], Ming Liu[1*], and Jianghong Gong[2*]

[1] *Fujian Provincial Key Laboratory of Terahertz Functional Devices and Intelligent Sensing, School of Mechanical Engineering and Automation, Fuzhou University, Fuzhou 350108, China;*

[2] *State Key Laboratory of New Ceramics and Fine Processing, School of Materials Science and Engineering, Tsinghua University, Beijing 100084, China*

Received April 10, 2024; accepted May 14, 2024; published online August 22, 2024

The reduced elastic modulus E_r and indentation hardness H_{IT} of various brittle solids including ceramics, semiconductors, glasses, single crystals, and laser material were evaluated using nanoindentation. Various analysis procedures were compared such as Oliver & Pharr and nominal hardness-based methods, which require area function of the indenter, and other methods based on energy, displacement, contact depth, and contact stiffness, which do not require calibration of the indenter. Elastic recovery of the imprint by the Knoop indenter was also utilized to evaluate elastic moduli of brittle solids. Expressions relating H_{IT}/E_r and dimensionless nanoindentation variables (e.g., the ratio of elastic work over total work and the ratio of permanent displacement over maximum displacement) are found to be nonlinear rather than linear for brittle solids. The plastic hardness H_p of brittle solids (except traditional glasses) extracted based on E_r is found to be proportional to $E_r\sqrt{H_{IT}}$.

Brittle solids, Nanoindentation, Elastic modulus, Hardness, Elastic recovery of Knoop imprint

Citation: Z. Xu, M. Liu, and J. Gong, Characterization of elastic modulus and hardness of brittle solids by instrumented indentation, Acta Mech. Sin. 41, 424095 (2025), https://doi.org/10.1007/s10409-024-24095-x

1. Introduction

Mechanical properties (e.g., elastic modulus [1-7], hardness [8-11], fracture toughness [12-14], and cracking resistance [15,16]) of various materials are essential for their structural applications [17-22]. Elastic modulus represents the obstacle in elastic deformation of material [23], and the alloys used as biomedical implants should have a relatively low elastic modulus close to that of the bone [24,25]. Hardness, which can be used to characterize the resistance to slip process, is a useful indicator of irreversible deformation [26], and the hardness of perfectly plastic material is directly related to the yield stress, which does not hold for brittle solids that fracture before yielding. Elastic modulus can be measured by various methods such as uniaxial tensile test, resonant ultrasound spectroscopy [27], thermal conductivity approach (for silica aerogels) [28], bending test [29], and nanoindentation [10,30]. Elastic modulus and hardness of brittle solids can be well characterized by nondestructive instrumented indentation [31], whose sample preparation is much simpler than other methodologies (e.g., uniaxial tensile and three-point bending tests), as only surfaces of good finish are required [32]. Moreover, indentation tests can be carried out precisely on the preselected area to avoid the effect of defects (e.g., porosity and cracking) in brittle solids, elastic modulus and indentation hardness of individual phase can thus be estimated [33], and mechanical property maps (e.g., hardness and elastic modulus) by grid indentation are fingerprints of local microstructure, element content, and crystallographic orientation [34].

Nanoindentation has been extensively used to evaluate localized micromechanical properties (e.g., bonding behavior [35], interface decohesion [36,37], stress-strain response [38], kinematic hardening parameters [39], creep [40-42], hardness [43,44], fracture [45,46], and viscoelastic-plastic properties [47,48]) and mechanisms (e.g., phase transfor-

*Corresponding authors. E-mail addresses: mingliu@fzu.edu.cn (Ming Liu); gong@tsinghua.edu.cn (Jianghong Gong)
Executive Editor: Qunyang Li

mation [49], ductile-brittle transition [50], structural alteration [51], fatigue crack growth [52], and local contact fatigue [53]) of various materials (e.g., brittle solids [54,55], metallic glasses [56-59], metals [60-65], polymers [66-69], piezoelectric materials [70-72], biomaterials [73,74], thin films [71,75-78], composites [37,79-81], and biomaterials [82,83]). Multicyclic indentation tests were carried out on brittle glasses to investigate the pop-in event and fracture toughness based on indentation-induced cracking [84]. Nanoindentation has been used to investigate the effect of hydrogen ion implantation on elastic modulus, indentation hardness, fracture behaviors, and phase transformation of 4H-SiC [85]. Photo-indentation has been used to assess the effect of light on dislocation-mediated plasticity in single crystals ZnO [86]. Nano- and micro-indentation has been used to evaluate the mechanical properties of silicon oxycarbide of various structures [87]. Nanoindentation has been used to unravel the elastic-plastic transition of lithium metasilicate/disilicate glass-ceramics [88]. Nanoindentation has been used to obtain elastic modulus of brittle solids based on the indirect indentation method [89]. A significant uncertainty can be introduced when an area function pre-calibrated on a reference material is applied to other material, whose mechanical properties differ significantly from the reference material [90], since many factors (e.g., pile-up [91], pop-in [92], residual stress [93-95], surface effects [96], friction [97,98], and zero point of initial contact [99]) can affect the projected contact area that depends on both indenter geometry and material properties [100-102]. Thus, many alternative methods without requiring the projected contact area have thus been proposed based on dimensionless relationships among nanoindentation variables [103], while a comprehensive comparison of various methods for estimating elastic modulus and indentation hardness of brittle solids is still lacking.

In the present work, instrumented indentation with Berkovich indenter was used to characterize various brittle solids including ceramics, glasses, semiconductors, single crystals, and laser material. Elastic modulus and indentation hardness were analyzed by various methods such as Oliver & Pharr (OP) and nominal hardness-based methods, which require area function of the indenter, and other methods that do not require calibration of the indenter including energy-based, displacement-based, and contact stiffness-based methods. The primary focus was on comparing different methodologies and their applicability to brittle solids, paving the way for characterization of micromechanical properties of brittle solids by instrumented indentation that does not need the calibration of the indenter. The relationships between the ratio of indentation hardness H_{IT} over reduced modulus E_r and the dimensionless nanoindentation variables (i.e., the ratio of elastic work W_e over the total work W_t, and the ratio of the plastic displacement h_p or contact depth h_c over the maximum displacement h_{max}) for brittle solids can be expressed by nonlinear rather than linear functions. Elastic modulus calculated by the elastic recovery of the hardness imprint of Knoop indenter under low loads in the absence of indentation-induced damage can also be used to assess elastic modulus of brittle solids. It is found for the first time that plastic hardness H_p [104] calculated by E_r is proportional to $E_r\sqrt{H_{IT}}$ for brittle solids, except for traditional glasses.

2. Analysis methods

2.1 Oliver & Pharr (OP) method

Reduced plane strain modulus E_r of the contact, which represents the combination of plane strain moduli of the sample and the indenter, and indentation hardness H_{IT} can be calculated from the contact stiffness S (i.e., the initial slope of the unloading curve at the maximum indentation displacement h_{max}) and as the mean contact pressure at the maximum indentation load F_{max}, respectively [105]:

$$E_r = 1\Big/\left(\frac{1-\nu^2}{E_{IT}}+\frac{1-\nu_i^2}{E_i}\right)=\frac{\sqrt{\pi}S}{2\beta\sqrt{A_p(h_c)}},\ H_{IT}=\frac{F_{max}}{A_p(h_c)}, \quad (1)$$

where h and F are the indentation displacement and load, respectively, with the subscript "max" indicating the maximum value; E_{IT} and ν are elastic modulus and Poisson's ratio, respectively, of the sample; E_i = 1141 GPa, and ν_i = 0.07 are elastic modulus and Poisson's ratio, respectively, of the diamond indenter; β = 1.034 is the correction factor for Berkovich indenter lacking axial symmetry [106]; and both h_p and m are curve fitting parameters of the unloading curve by a simple power law function as [107]

$$F=F_{max}\left(\frac{h-h_p}{h_{max}-h_p}\right)^m,\ S=\left.\frac{dF}{dh}\right|_{h_{max}}=\frac{mF_{max}}{h_{max}-h_p},$$
$$h_c=h_{max}-\varepsilon\frac{F_{max}}{S}, \quad (2)$$

where h_p can be regarded as permanent indentation displacement after complete unloading; m is an exponent normally ranging between 1.2 and 1.7 [108,109]; ε is dependent on m [110]; and $A_p(h_c)$, which is the projected contact area (or the area function of the indenter), is determined by calibration on a standard fused silica ($F_{max} \le 100$ mN in order to avoid indentation-induced damage) with known elastic modulus and Poisson's ratio as a function of contact depth h_c with B-spline interpolation [106].

The unknown E_r and H_{IT} can also be obtained by solving the system of binary equations, and one of the two independent equations can be obtained from Eq. (1) [111]:

$$\frac{H_{IT}}{E_r^2}=\frac{4\beta^2F_{max}}{\pi S^2}. \quad (3)$$

The loading curve is related to H_{IT}/E_r [111], and can be expressed as [112]

$$F=\left(\frac{1}{\sqrt{24.5H_{IT}}}+\frac{\varepsilon}{2E_r}\sqrt{\pi H_{IT}}\right)^{-2}h^2, \quad (4)$$

where ε = 0.75 for Berkovich indenter.

2.2 Energy and displacement-based approaches

The elastic recovery work W_e can be calculated as the area under the unloading curve; the total deformation work W_t can be obtained by integrating the loading and holding segments of load-displacement curve [106]; and plastic deformation work W_p ($= W_t - W_e$) of indentation can be calculated as the net area enclosed by the loading and unloading curves [109]. Relationships among H_{IT}/E_r, W_e/W_t, and h_p/h_{max} have been extensively explored, and the various expressions of linear or nonlinear types reported in the literature are listed in Table 1 [91,111,113-118], and a robust expression relating H_{IT}/E_r with W_e/W_t or h_p/h_{max} for brittle solids requires further study. It is worth noting that the displacement-based Eqs. (14) and (16) are equivalent with exponent $m = 2$.

With Eqs. (3) and (10), E_r and H_{IT} can be simultaneously solved as

$$E_r = \frac{S^2}{F_{max}}\left\{2\beta\tan\theta\left[\frac{3m}{m+1}\left(\frac{W_e}{W_t}\right)^{-1} - \varepsilon\right]\right\}^{-1},$$
$$H_{IT} = \frac{S^2}{\pi F_{max}}\left[\tan\theta\frac{3m}{m+1}\left(\frac{W_e}{W_t}\right)^{-1} - \varepsilon\right]^{-2}, \tag{17}$$

which is named energy-based method. S^2/F_{max} can be assumed to be a constant that is dependent on material.

The normalized unloading curve (F/F_{max} vs. h/h_{max}) can be fitted with a quadratic polynomial function [119]:

$$\frac{F}{F_{max}} = \alpha_0 + \alpha_1\left(\frac{h}{h_{max}}\right) + \alpha_2\left(\frac{h}{h_{max}}\right)^2,$$
$$S = \left(\frac{dF}{dh}\right)_{h=h_{max}} = \frac{F_{max}}{h_{max}}(\alpha_1 + 2\alpha_2), \tag{18}$$

where α_0, α_1, and α_2 are dimensionless fitting parameters, which are normally independent of the maximum load [120].

2.3 Contact stiffness-based method

The relationship $S^2 = c_0 + c_1 h_c + c_2 h_c^2$ can be transformed into [119]

$$S = \sqrt{\frac{c_2}{24.5}\left(\frac{24.5c_0}{c_2} + \frac{24.5c_1}{c_2}h_c + 24.5h_c^2\right)}. \tag{19}$$

Comparing Eqs. (1) and (19) with $c_0 = 0$, it is found that [119]

$$S = \sqrt{\frac{4\beta^2 E_r^2}{\pi}A_p(h_c)} = \sqrt{\frac{c_2}{24.5}\left(24.5h_c^2 + \frac{24.5c_1}{c_2}h_c\right)},$$
$$A_p(h_c) = 24.5h_c^2 + \frac{24.5c_1}{c_2}h_c,\ E_r = \frac{\sqrt{\pi}}{2\beta}\sqrt{\frac{c_2}{24.5}}, \tag{20}$$

Table 1 Relationships between W_e/W_t (or h_p/h_{max}) and H_{IT}/E_r

Expressions	Eq.	Indenter and reference	Type
$\frac{H_{IT}}{E_r} = \chi\frac{W_e}{W_t}$: $1/\chi = \lambda(1+\gamma) = 5.736$, $\gamma = 0.27$, $\lambda = 1.5\tan\theta + 0.327 = 4.02$, $\theta = 70.3°$, for $\frac{h_p}{h_{max}} > 0.4$ or $\frac{W_p}{W_t} > 0.2$	(5)	Conical [111,113,114] ($60° \le \theta \le 80°$)	Linear
$\frac{H_{IT}}{E_r} = \chi\frac{W_e}{W_t}$: $1/\chi = \begin{cases}7.30, & \text{for } W_e/W_t < 0.15,\\ 5.17, & \text{for } W_e/W_t \geqslant 0.15\end{cases}$	(6)	Conical [91] ($\theta = 70.3°$)	Linear
$\frac{H_{IT}}{E_r} = \chi\frac{W_e}{W_t}$: $1/\chi = 4.678$	(7)	Berkovich [115]	Linear
$\frac{H_{IT}}{E_r} = \chi\frac{W_e}{W_t}$: $1/\chi = 2\tan\theta = 5.59$	(8)	Berkovich [116]	Linear
$\frac{W_e}{W_t} = \left[\frac{\varepsilon}{2} + \frac{\beta}{\pi\tan\theta}\left(\frac{H_{IT}}{E_r}\right)^{-1}\right]^{-1}$	(9)	Berkovich [116]	Nonlinear
$\frac{W_e}{W_t} = \frac{3m\pi}{2\beta(m+1)}\left[\left(\tan\theta\frac{H_{IT}}{E_r}\right)^{-1} + \frac{\pi\varepsilon}{2\beta}\right]^{-1}$	(10)	Berkovich [117]	Nonlinear
$\frac{h_p}{h_{max}} = 1 - \Theta\frac{H_{IT}}{E_r}$: $\Theta = \lambda = 4.02$	(11)	Berkovich [114]	Linear
$\frac{h_p}{h_{max}} = 1 - \Theta\frac{H_{IT}}{E_r}$: $\Theta = 2\tan\theta = 5.59$	(12)	Berkovich [116]	Linear
$\left(\frac{h_p}{h_{max}}\right)^2 = 1 - 2\left(\frac{\Upsilon_E}{\Upsilon_H}\right)^2\tan\theta\frac{H_{IT}}{E_r}$, $\frac{\Upsilon_E}{\Upsilon_H} = 1.18$	(13)	Berkovich [114]	Nonlinear
$\frac{h_p}{h_{max}} = 1 - \left[\frac{\varepsilon}{2} + \frac{\beta}{\pi\tan\theta}\left(\frac{H_{IT}}{E_r}\right)^{-1}\right]^{-1}$	(14)	Berkovich [116]	Nonlinear
$\frac{h_p}{h_{max}} = \left[1 + \left(\frac{2}{\tan\theta}\frac{H_{IT}}{E_r}\right)^{1/2}\right]^{-1}$	(15)	Berkovich [118]	Nonlinear
$\frac{h_p}{h_{max}} = 1 - \frac{m\pi}{2\beta}\left[\left(\tan\theta\frac{H_{IT}}{E_r}\right)^{-1} + \frac{\pi\varepsilon}{2\beta}\right]^{-1}$	(16)	Berkovich [117]	Nonlinear

a): For Berkovich indenter, equivalent cone apex semi-angle $\theta = 70.3°$; geometry correction factor $\beta = 1.034$; intercept factor $\varepsilon = 0.75$; Υ_E and Υ_H are parameters that are sensitive to the degree of surface sink-in or pile-up.

where $24.5h_c^2$ is the projected contact area of the ideal Berkovich indenter.

Substituting Eq. (20) into Eq. (1) gives

$$H_{IT} = \frac{F_{max}}{A_p(h_c)} = \frac{F_{max}}{24.5\left[h_c^2 + (c_1/c_2)h_c\right]}, \tag{21}$$

where h_c can be obtained by OP method Eq. (2).

2.4 Nominal hardness-based method

Martens hardness, which is defined at the maximum indentation depth under the maximum applied load, is less affected by the material's viscoelastic and optical properties [121], and is equivalent to nominal hardness H_n. The ratio of nominal hardness H_n over combined modulus E_c is a function of W_e/W_t [122]:

$$\frac{H_n}{E_c} = \sum_{i=1}^{6} a_i \left(\frac{W_e}{W_t}\right)^i, \quad H_n = \frac{F_{max}}{A_{max}},$$
$$\frac{1}{E_c} = \frac{(1-\nu^2)}{E_{IT}} + 1.32\frac{\left(1-\nu_i^2\right)}{E_i}, \tag{22}$$

where the coefficients a_1-a_6 are 0.16716, −0.13875, 0.06215, 0.01568, −0.04784, and 0.01878, respectively; H_n is calculated as the ratio of the maximum load F_{max} over the projected contact area A_{max} determined at h_{max} and considering the tip roundness [123]:

$$A_{max} = \frac{F_{max}}{H_n} = \frac{F_{max}}{E_c \sum_{i=1}^{6} a_i (W_e/W_t)^i}$$
$$= 24.5(h_{max} + \Delta h)^2, \text{ for } h_{max} > h_0, \tag{23}$$

where $\theta = 70.3°$ for Berkovich indenter, Δh is the distance from the apex of the perfect indenter to the tip of the rounded indenter, see the inset of Fig. 1, $h_0 = R(1 - \sin\theta)$ is the sphere-to-cone transition distance, and $R = \Delta h \sin\theta/(1 - \sin\theta)$ is tip radius of Berkovich indenter [106,109]. To characterize the indenter tip, W_e and W_t under various F_{max} ($F_{max} \le 100$ mN to avoid indentation-induced damage) were obtained by indenting fused silica with known plane strain modulus $E^* = E/(1 - \nu^2)$ of 75.3 GPa [109] and combined modulus E_c of 69.2 GPa, and thus A_{max} can be calculated by Eq. (23). $\Delta h = 25$ nm ($R = 402$ nm, and $h_0 = 23.5$ nm) can be obtained by linear fitting of $(A_{max}/24.5)^{0.5}$ vs. h_{max} with Eq. (23).

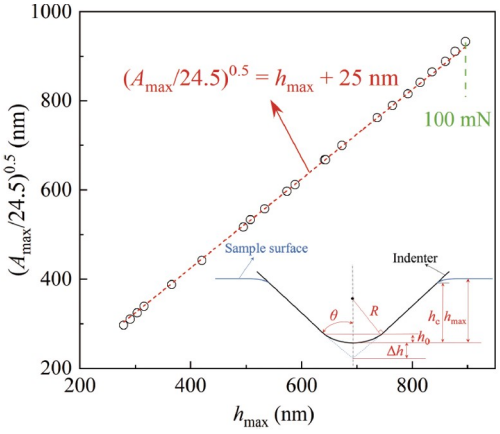

Figure 1 Characterization of indenter tip by fitting $(A_{max}/24.5)^{0.5}$ vs. h_{max} curve with Eq. (23). The inset shows schematic illustration of equivalently conical indenter with a spherical tip.

With known F_{max} and A_{max}, H_n can be calculated, and E_c can be computed by Eq. (22) with a constant value of W_e/W_t. Then, E_r can be computed by substituting Eq. (22) into Eq. (1):

$$\frac{1}{E_r} = \frac{1}{E_c} - 0.32\frac{1-\nu_i^2}{E_i}, \tag{24}$$

where $E_i = 1141$ GPa, and $\nu_i = 0.07$ are elastic modulus and Poisson's ratio of the diamond indenter, respectively.

2.5 Plastic hardness

Assume "springs in series" for elastic (i.e., h_{el}) and plastic (i.e., h_{pl}) deformation, which contributes to the total contact depth as mechanical elements in series, and the loads in the elastic (i.e., P_{el}) and plastic (i.e., P_{pl}) elements are equal for elements in series [104,124-126]:

$$h_c = h_{el} + h_{pl}, \quad P_{el} = 4.4E_r h_{el}^2 = P = P_{pl} = 24.5H_p h_{pl}^2, \tag{25}$$

where H_p is the term quantifying the resistance to permanent deformation, and reduced modulus E_r is used considering the elastic deformation of both the indenter and the sample in the current work, while the plane strain modulus $E^* = E/(1 - \nu^2)$ was used in the previous study without considering the elastically deformable indenter [104].

Assuming a perfect Berkovich indenter, the contact hardness H_{IT} can be calculated at peak load P_{max} as [105]

$$H_{IT} = \frac{P_{max}}{A_c} = \frac{P_{max}}{24.5h_c^2}. \tag{26}$$

Substituting $h_{el} = \sqrt{\frac{P_{max}}{4.4E_r}}$ and $h_{pl} = \sqrt{\frac{P_{max}}{24.5H_p}}$ by Eq. (25) into Eq. (26), it is found that [124]

$$H_{IT} = \frac{\left[(4.4E_r)^{-1/2} + (24.5H_p)^{-1/2}\right]^{-2}}{24.5}, \tag{27}$$

which can be rearranged in terms of plastic hardness H_p:

$$H_p = \frac{\left[(24.5H_{IT})^{-1/2} - (4.4E_r)^{-1/2}\right]^{-2}}{24.5}. \tag{28}$$

3. Experimental procedures

3.1 Materials

The mechanical properties (i.e., Poisson's ratio ν, elastic

modulus E, indentation hardness H_{IT}, and fracture toughness K_C in the literature) of 12 different brittle solids studied are listed in Table 2 [106,109,127-146]: 9 brittle solids are commercially available including Al_2O_3, Si_3N_4, ZrO_2, Si (111), SiC, K9 glass, soda-lime-silica (SLS) glass, fused silica, and laser material ZnSe, and 3 brittle solids including dielectric ceramic $BaO\text{-}Sm_2O_3\text{-}5TiO_2$ (BST), single crystal $ScAlMgO_4$ (SCAM), and single crystal $Y_{2.88}Dy_{0.12}Al_5O_{12}$ (YDAG) were prepared in the laboratory.

$BaO\text{-}Sm_2O_3\text{-}5TiO_2$ (BST) ceramic [22] was synthesized by the solid-state reaction method with the regent grade powders $BaCO_3$, TiO_2, Sm_2O_3 (purity > 99.99 wt.%), which were firstly wet ball-milled for 12 h in a nylon jar using deionized water and zirconia balls, passed through an 80 mesh sieve after drying at 130 °C, and calcined in ambient atmosphere for 4 h at 1170 °C with heating rate of 10 K/min in the muffle furnace, followed by natural air cooling inside the furnace. Then, the cylindrical samples with the dimensions of 12 mm in diameter and 6 mm in height were formed by uniaxially pressing the powder mixtures into a cylindrical mold under the pressure of 180 MPa. The BST samples were prepared by sintering at 1350 °C for 4 h in the furnace at a heating rate of 3 K/min (followed by natural air cooling inside the furnace) according to the following reaction:

$$BaO+5TiO_2+Sm_2O_3 \rightarrow BaO\text{-}Sm_2O_3\text{-}5TiO_2. \quad (29)$$

Single crystal SCAM was synthesized by the floating zone (FZ) method using a FZ furnace (FZD0192, Canon Machinery Inc.) with Sc_2O_3, Al_2O_3, MgO (purity > 99.99 wt.%), which was firstly mixed under the stoichiometric ratio, and formed into a cylinder rod by applying the hydrostatic pressure [147]. Then, the cylinder rod was sintered at 1500 °C for 8 h in ambient atmosphere. The sintered rod was loaded into the FZ furnace to conduct crystal growth (the pulling rate was 3-5 mm/h, the rotation rate was 20 r/min, and the heat radiation source of the FZ furnace was halogen lamp) according to the following reaction [148]:

$$Al_2O_3+2MgO+Sc_2O_3 \rightarrow 2ScAlMgO_4. \quad (30)$$

Single crystal YDAG [149] was prepared by the solid-phase sintering process with Y_2O_3, Al_2O_3, and Dy_2O_3 (purity > 99.99 wt.%), which were mixed by a wet ball milling with alcohol in a mill machine (MITR-YXQM-4L, MITR) for 24 h, and were weighed according to Ref. [149]:

$$2.88Y_2O_3+5Al_2O_3+0.12Dy_2O_3 \rightarrow 2Y_{2.88}Dy_{0.12}Al_5O_{12}. \quad (31)$$

The powder mixtures were then dried and pressed under uniaxial pressing of 10 MPa into tablets, which were loaded into crucibles and calcined for 48 h in a muffle furnace at 1450 °C, followed by natural air cooling inside the furnace, and finally placed into an iridium crucible under a protective atmosphere of 99.99 vol. % N_2, and were grown into single crystals by the Czochralski method [149].

The surfaces of specimens including Al_2O_3, Si_3N_4, ZrO_2, BST, SCAM, and YDAG were sequentially ground using silicon carbide water-proof abrasive papers from 600# to 3000# grits followed by manually polishing with diamond paste of 1.0 μm, and ion beams on Leica EM TIC 3X-Ion Beam Slope Cutter was used as the final finishing. The surfaces of commercially available semiconductors (i.e., Si (111) and SiC), glasses (i.e., K9 glass, SLS glass, and fused silica), and ZnSe are sufficiently smooth, see the optical microscopy in the insets of Fig. 2, and do not need further surface preparation. Before indentation tests, the sample surfaces were ultrasonically cleaned to remove polishing abrasives and other impurities.

3.2 Experiments

Nanoindentation tests were performed on nanoindentation tester (NHT^2 of Anton Paar) under various loads with loading/unloading times of 30 s and holding time of 10 s. Berkovich indenter, which has face angle α of 65.27°, resulting in the same ratio of the projected contact area over the contact depth as that of Vickers indenter [109], was used. Knoop hardness tests were conducted under various loads

Table 2 Mechanical properties of various brittle solids reported in the literature [a)]

Material	Poisson's ratio, ν	Elastic modulus, E (GPa)	Hardness, H_{IT} (GPa)	Fracture toughness, K_C (MPa·m$^{1/2}$)
Al_2O_3	0.24 [127]	305 [128]	19.1 [128]	4.6 [128]
Si_3N_4	0.27 [129]	300 [128]	18.5 [128]	4.0 [128]
ZrO_2	0.3 [130]	233 [131]	15.7 [132]	7-10 [133]
BST	0.2 [134]	230 [134]	9 [134]	2.9 [134]
Si (111)	0.22 [135]	206 [136]	9 [137]	0.91 [138]
SiC	0.22 [139]	430 [139]	24.0 [128]	3.1 [129]
K9 glass	0.206 [109]	82 [109]	7.72 [109]	0.8 [140]
SLS glass	0.21 [141]	73 [128]	5.6 [128]	0.75 [128]
Fused silica	0.17 [106]	75.3 [106]	9.8 [106]	0.825 [142]
SCAM	0.2	204	14.0	–
ZnSe	0.3 [143]	71 [143]	1.5 [143]	0.9 [143]
YDAG	0.233 [144]	268 [145]	24.7 [145]	1.04 [146]

a): Elastic modulus and indentation hardness of SCAM (Poisson's ratio is assumed to be 0.2) were obtained by nanoindentation tests (Toray Research Center, Inc.)

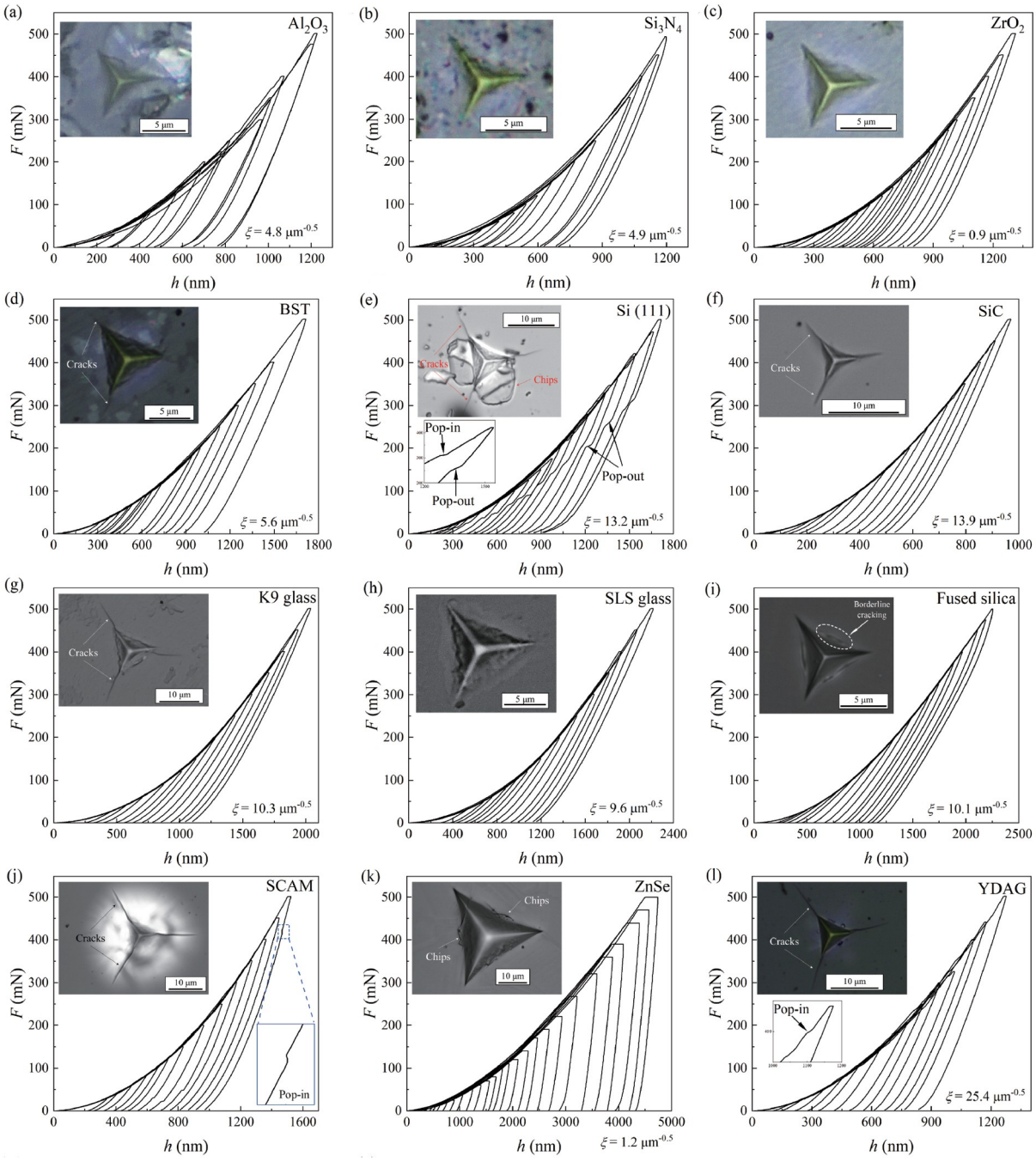

Figure 2 *F-h* curves of 12 brittle solids under various loads. (a) Al_2O_3, (b) Si_3N_4, (c) ZrO_2, (d) BST, (e) Si (111), (f) SiC, (g) K9 glass, (h) SLS glass, (i) fused silica, (j) SCAM, (k) ZnSe, and (l) YDAG. The insets show the optical images of residual indents at the maximum load F_{max} = 500 mN.

with holding time of 15 s.

Time-dependent mechanical properties of material can be characterized under a constant strain rate during nanoindentation tests [150,151]. The nanoindentation strain rate in nanoindentation lies between 0.01 s^{-1} and 0.10 s^{-1}, and is defined as the ratio over the increment rate and the instantaneous value of the indentation displacement, which is half of the ratio of the increment rate over the instantaneous value of the indentation load, while the strain rates of uniaxial tests are normally between 10^{-4} s^{-1} and 10^{-3} s^{-1}, and are differently defined by the change in the uniaxial strain with respect to time [152,153], and a shift of nanoindentation strain rate by a factor is required when applying nanoindentation to characterize the constitutive parameters obtained by uniaxial tests [154]. Nevertheless, a constant loading rate rather than a constant strain rate was used in the current study without considering the effect of strain rate, since mechanical properties of brittle solids can be assumed to be time-independent. Moreover, a constant strain rate is more difficult to maintain than a constant

loading rate, and the measurement under a constant loading rate is more accurate and reliable than that under a constant strain rate [108].

4. Results and discussion

4.1 Analysis by OP method

Figure 2 shows indentation load-displacement (*F*-*h*) curves of 12 brittle solids. The loading segments follow almost the same trace, and the slight deviation of loading curves of Al_2O_3 and Si_3N_4 under large loads is caused by their heterogeneous microstructure, see Fig. 2(a) and (b). The pop-in (or pop-out) in loading (or unloading) segment of single crystal Si (111) is attributed to phase transformation [155,156]. Sink-in prevails for Al_2O_3, Si_3N_4, Si (111), SiC, K9 glass, fused silica, and ZnSe, see the insets of Fig. 2(a), (b), (e), (f), (g), (i), and (k). Fused silica is damaged and permanently densified under large loads, resulting in the nose-like phenomenon in unloading segment due to its distinctive deformation mechanism [157,158]. ZnSe has the largest indentation size due to its soft and brittle nature [159,160], which is demonstrated by its low values of both hardness and fracture toughness, see Table 2, and has special deformation mechanisms (e.g., local lattice distortion at subsurface and phase transformation under relatively large stresses) [161,162].

Borderline cracks are observed for fused silica under large loads, as expected [163]. Radial cracks emanating at the indent corners appear for BST ceramic, Si (111), SiC, K9 glass, SCAM, and YDAG, and chips with fragmentation are formed around the indent region on the surface under 500 mN for Si (111). As the indentation load increases, cracking appears for some materials, and the smallest applied load that can induce cracking is regarded to be the critical load F_c for crack initiation, which is listed in Table 3. F_c cannot be obtained for some materials in the absence of visible surface cracking under the loads ($\leq$ 500 mN) applied in the current study.

The white area beneath the residual indentation imprint of SCAM shown in the inset of Fig. 2(j), is attributed to lateral cracking that is reported in various brittle glasses [164,165] and cleavage. Figure 2(l) shows that the pop-in events on the loading segment of *F*-*h* curves of YDAG, which has been previously reported for the YAG single crystal [145], and is associated with the dislocation nucleation and subsequent plane slips [145,166].

The unloading segment of *F*-*h* curves were fitted by OP method Eq. (2) with the fitting range from 98% F_{max} to 40% F_{max} for most materials except Si (111), whose fitting range is 98%F_{max} to 60%F_{max}, since Si (111) exhibits pop-out due to phase transformation [155,156]. Figure 3 displays the relationships among various indentation variables (i.e., E_{IT}, H_{IT}, W_e, W_t, h_p, h_{max}, h_c, m, S^2, $h_p/F_{max}^{0.5}$, $W_p/F_{max}^{1.5}$, and F_{max}) for the 12 brittle solids.

Figure 3(a) and (b) show that under small loads (F_{max} < 15 mN), the values of E_{IT} and H_{IT} vary with F_{max}, and the data in this regime were discarded. Although the values of H_{IT} of brittle solids under small loads show indentation size effect (ISE), which is normally manifested by an increase in hardness with the decrease in the indentation displacement (or indentation area, load [167]) and is widely reported for various materials (e.g., single crystals [168,169], ceramics [170,171], composites [172,173], polymers [174], metallic glasses [175,176], and high entropy carbides [172]), size effect of constitutive properties of material is hard to characterize by nanoindentation, since ISE can be attributed to many factors such as materials (e.g., microstructure [174], surface undulation [101,177], and strain hardening [178]), the indenters (e.g., tip irregularity [101]), and friction between the indenter and the sample surface [139]. Different models without considering the intrinsic size effect of constitutive properties of material have been proposed to describe ISE such as Meyer's law [179], Hays and Kendall's approach [180], elastic/plastic deformation model [181], and the proportional specimen resistance model [182,183]. Under large loads (F_{max} > 15 mN), both E_{IT} and H_{IT} of most ma-

Table 3 Indentation results of various brittle solids by OP method

Material	E_{IT} (GPa)	E_r (GPa)	H_{IT} (GPa)	h_p/h_{max}	h_c/h_{max}	W_e/W_t	m	F_{max}/S^2 (nm^2/mN)	$S/(F_{max}/h_{max})$	F/h^2 (mN/μm^2)	F_c (mN)
Al_2O_3	341	252	21.9	0.63	0.8	0.43	1.38	208	3.7	343	–
Si_3N_4	303	252	19.6	0.57	0.8	0.53	1.59	219	3.7	350	–
ZrO_2	254	209	16.9	0.61	0.8	0.45	1.47	243	3.7	303	–
BST	260	198	16.2	0.6	0.77	0.46	1.32	518	3.4	187	250
Si (111)	189	182	12	0.49	0.81	0.5	2	366	3.8	182	50
SiC	534	324	43.1	0.55	0.74	0.54	1.34	203	2.9	562	100
K9	84	80	8.2	0.53	0.75	0.57	1.39	939	3	124	250
SLS	74	72	7.2	0.54	0.75	0.57	1.39	1074	3	107	–
Fused silica	69	73	8.3	0.49	0.72	0.58	1.24	1327	2.7	105	100
SCAM	229	179	12	0.63	0.84	0.41	1.66	221	4.4	223	80
ZnSe	78	73	1.1	0.9	0.96	0.079	1.7	128	17.5	27	200
YDAG	320	227	26.4	0.66	0.8	0.41	1.31	215	3.8	325	100

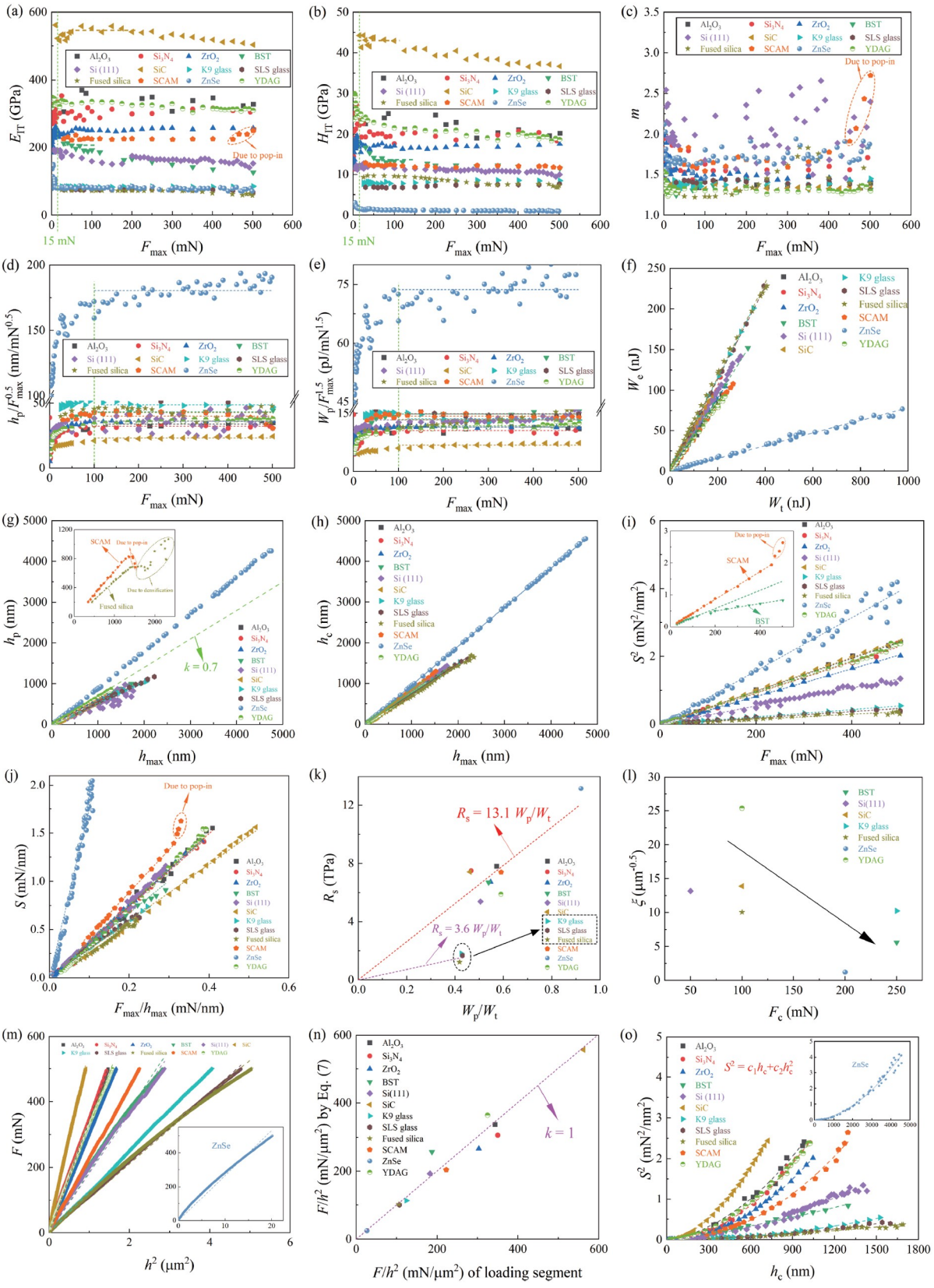

Figure 3 Relationships among various indentation variables for the 12 brittle solids: (a) E_{IT} vs. F_{max}, (b) H_{IT} vs. F_{max}, (c) m vs. F_{max}, (d) $h_p/F_{max}^{0.5}$ vs. F_{max}, (e) $W_p/F_{max}^{1.5}$ vs. F_{max}, (f) W_e vs. W_t, (g) h_p vs. h_{max}, (h) h_c vs. h_{max}, (i) recovery resistance R_s (= $2.263E_r^2/H_{IT}$) vs. W_p/W_t, (j) S^2 vs. F_{max}, (k) S vs. F_{max}/h_{max}, (l) brittleness index ξ (= H_{IT}/K_C) vs. critical load F_c listed in Table 3 based on surface cracking, (m) F vs. h^2 during loading segment (the results were measured under F_{max} = 500 mN), (n) F/h^2 calculated by Eq. (4) vs. F/h^2 of loading segment by curve fitting, and (o) S^2 vs. h_c.

terials (except BST and SiC) can normally be assumed to be constant, which are widely reported [56,106,109,119]; the decrease in E_{IT} and H_{IT} of BST and SiC are caused by the indentation-induced damage/cracking, and the average values of the stable state under intermediate loads are the reasonable values; the small increase in E_{IT} of SCAM under large loads can be explained by noting the pop-in during unloading, see Fig. 3(b). The constant values of H_{IT} and E_r calculated from the stable state by OP method Eq. (1) are listed in Table 3. The values of H_{IT}/E_r of K9 glass and fused silica are almost the same as those reported in the literature (i.e., 0.10 for K9 glass [109], 0.13 for fused silica [106]).

Figure 3(c) shows that the values of power law exponent m of most materials lie within the normal range ($1.2 < m < 1.7$) [108,109]. Values of m of Si (111) are larger than 2, and show large scattering, which can be attributed to phase transformation; the increase in m of SCAM under large loads is caused by the pop-ins in unloading segment. Figure 3(d) and (e) show that both $h_p/F_{max}^{0.5}$ and $W_p/F_{max}^{1.5}$ increase as F_{max} increases with the increasing rate becoming progressively smaller, and both can be approximated to be constant as the plastic deformation plays the dominating role. The proportional coefficients and constant values of the 12 brittle solids studied are listed in Table 3.

Figure 3(f)-(j) show that proportional relationships can be approximated between elastic work W_e and total indentation work W_t, between h_p (or h_c) and h_{max}, between S^2 and F_{max}, and between S and F_{max}/h_{max}. The proportional correlations between h_{max} and h_p (or h_c) have been widely reported [106,109,184,185], and h_p/h_{max} are smaller than 0.7 for most materials (except for ZnSe), indicating the absence of pile-up [186], which is consistent with the observations of imprints, see the insets in Fig. 2; ZnSe with h_p/h_{max} larger than 0.7 also exhibits no pile-up, see Fig. 2(j), which is attributed to its soft brittleness [159]. The sudden change in h_p/h_{max} (or h_c/h_{max}) for fused silica and SCAM under large loads or displacements is attributed to the nose-like phenomenon and pop-in, respectively, during unloading.

The capacity of energy dissipation during indentation increases with the increase in E_r^2/H_{IT} [157], and the recovery resistance R_s (= $2.263E_r^2/H_{IT}$ for Berkovich indenter) [157] can be used as an indicator of energy dissipation (or plastic work) during indentation. Figure 3(k) shows that although R_s can be regarded to be proportional to W_p/W_t, the proportionality depends on the type of brittle solid, and the three traditional glasses (K9, SLS, and fused silica) deviate from other ceramics, laser material, and semiconductors, since the values of F_{max}/S^2 of the three traditional glasses are much larger than those of other brittle materials, see Table 3, which is associated with the amorphous microstructure of traditional glasses. ZnSe with the largest plastic deformation component exhibits the largest R_s; and fused silica with the smallest plastic deformation component exhibits the smallest R_s.

The brittleness index ξ (= H_{IT}/K_C), indicative of the order of brittleness, is defined as the ratio of hardness over fracture toughness [187,188]. ξ calculated with H_{IT} in Table 3 and K_C in Table 2 are displayed in Fig. 3(l), which shows that ξ normally decreases as the critical load F_c increases, since a smaller ξ corresponds to a lower brittleness, which requires a larger F_c to induce cracking [187,188]. ZnSe exhibits the lowest brittleness due to the effect of metallic element Zn of ductility, and YDAG has the highest brittleness due to its low machinability [145]. K_C of SCAM is unavailable, and thus ξ of SCAM is not shown in Fig. 3(j). Figure 3(m) shows that F can be assumed to be proportional to h^2 during loading.

Figure 3(n) shows that values of F/h^2 calculated by Eq. (4) with H_{IT} and E_r listed in Table 3 are almost the same as those by curve fitting of loading segment, validating the applicability of Eq. (4) to brittle solids. Figure 3(o) shows that S^2 nonlinearly increases with the increase in h_c, and a quadratic polynomial function can be used to express their relationship: $S^2 = c_0 + c_1 h_c + c_2 h_c^2$ [119] (c_0, c_1, and c_2 are fitting parameters; constant term c_0 can be normally regarded to be zero).

4.2 Analysis by energy and displacement-based approaches

The energy-based relationship Eq. (10) and displacement-based Eq. (16) are equivalent provided that $W_e/W_t = 3(1 - h_p/h_{max})/(m + 1)$, which can be validated by the proportional curve fitting of W_e/W_t vs. $(1 - h_p/h_{max})/(m + 1)$, as shown in Fig. 4.

Figure 5(a) shows that W_e/W_t is not proportional to H_{IT}/E_r for brittle materials, and Eqs. (5)-(8) listed in Table 1 showing proportional relationships between W_e/W_t and H_{IT}

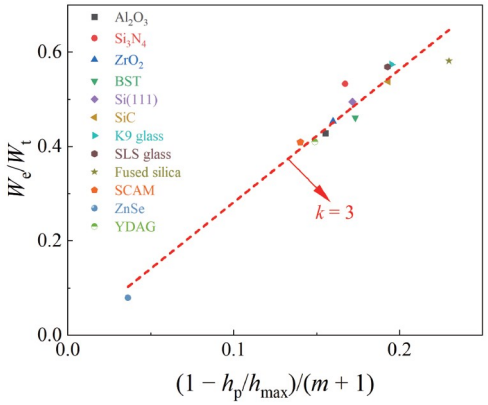

Figure 4 Variation of W_e/W_t with $(1 - h_p/h_{max})/(m + 1)$ for brittle solids.

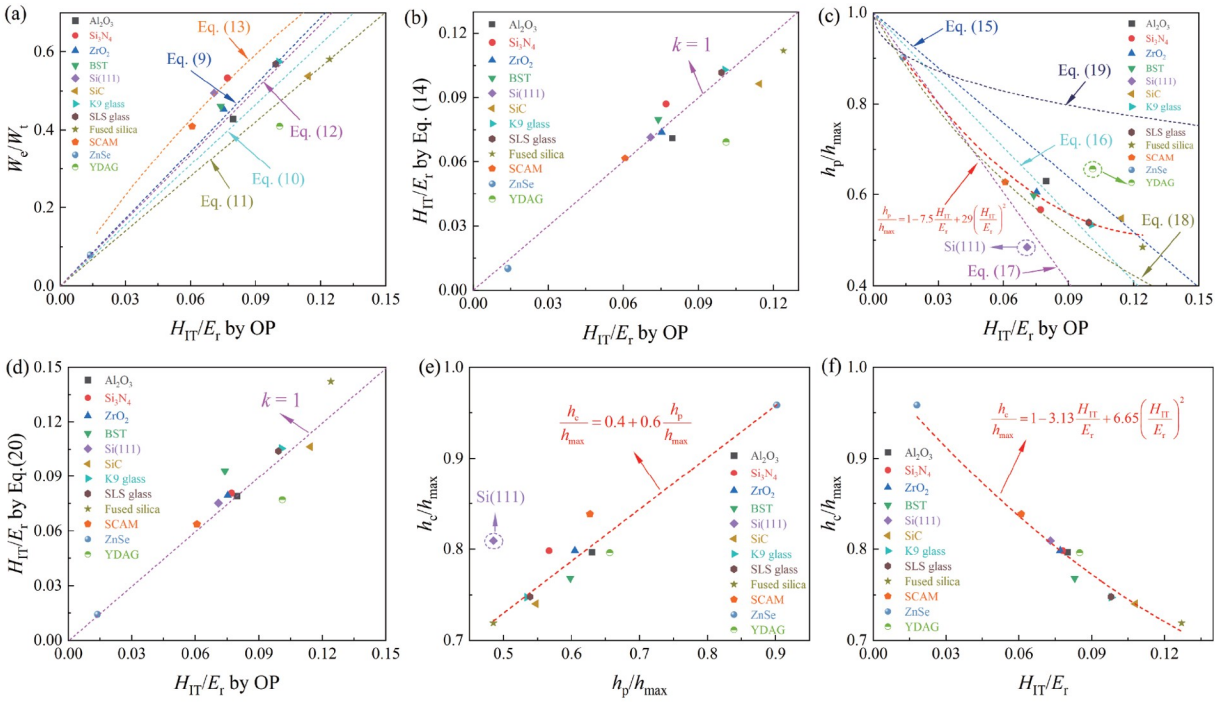

Figure 5 Relationships among normalized indentation variables: (a) W_e/W_t vs. H_{IT}/E_r, (b) comparison of H_{IT}/E_r calculated by Eq. (10) and OP method Eq. (1), (c) h_p/h_{max} vs. H_{IT}/E_r, (d) H_{IT}/E_r by Eq. (16) and those by OP method Eq. (1), (e) h_c/h_{max} and h_p/h_{max}, and (f) h_c/h_{max} and H_{IT}/E_r. The outliers encircled, such as fused silica in (a), and Si (111) and YDAG in (c), are not considered for curve fitting.

/E_r are inapplicable to brittle solids, and a large deviation of the data from the nonlinear prediction by Eq. (9) can be seen for some brittle materials. Values of H_{IT}/E_r obtained by Eq. (10) with m and W_e/W_t in Table 3 are compared well with those by OP method, see Fig. 5(b), indicating that the nonlinear expression, applicable to various materials spanning from brittle ceramics to ductile metals [103], is most suitable for the investigation of indentation hardness and elastic modulus of brittle solids. Moreover, the unloading exponent m plays a significant role in the relation between W_e/W_t and H_{IT}/E_r, as shown in Eq. (10).

Figure 5(c) shows that h_p/h_{max} is not proportional to H_{IT}/E_r for brittle materials, and Eqs. (11) and (12) listed in Table 1 showing proportional relationships between h_p/h_{max} and H_{IT} /E_r are inapplicable to brittle solids, and a large deviation of the data from the nonlinear prediction by Eqs. (13)-(15) can be seen for some brittle materials. A quadratic polynomial with the constant term of 1 can be used to express the dependence of h_p/h_{max} on H_{IT}/E_r for most materials except Si (111) and YDAG:

$$\frac{h_p}{h_{max}} = 1 - 7.5\frac{H_{IT}}{E_r} + 29\left(\frac{H_{IT}}{E_r}\right)^2. \tag{32}$$

The deviation of Si (111) and YDAG from the prediction is attributed to phase transformation of Si [155,156] and the largest brittleness index (i.e., ξ = 25.4 μm$^{-0.5}$) of YDAG, respectively. With m and h_p/h_{max} in Table 3, values of H_{IT}/E_r calculated by Eq. (16) are almost the same as those by OP method, as shown in Fig. 5(d). With Eqs. (3) and (16), E_r and H_{IT} can be obtained based on h_p/h_{max}:

$$E_r = \frac{S^2}{F_{max}}\left\{2\beta\tan\theta\left[\left(1-\frac{h_p}{h_{max}}\right)^{-1}m-\varepsilon\right]\right\}^{-1},$$
$$H_{IT} = \frac{S^2}{\pi F_{max}}\left\{\tan\theta\left[\left(1-\frac{h_p}{h_{max}}\right)^{-1}m-\varepsilon\right]\right\}^{-2}, \tag{33}$$

which is named displacement-based method.

Figure 5(e) shows a linear relationship between h_c/h_{max} and h_p/h_{max} obtained by linear fitting the variables under various loads:

$$\frac{h_c}{h_{max}} = 0.4 + 0.6\frac{h_p}{h_{max}}, \tag{34}$$

where the sum of intercept and slope is 1, which was also reported in the previous study [103].

Figure 5(f) shows that a quadratic polynomial function can be used to describe the relationship between h_c/h_{max} and H_{IT}/E_r:

$$\frac{h_c}{h_{max}} = 1 - 3.13\frac{H_{IT}}{E_r} + 6.65\left(\frac{H_{IT}}{E_r}\right)^2. \tag{35}$$

Figure 6 shows the variations of fitting parameters α_0, α_1, and α_2 with F_{max}: α_0 and α_2 are positive; while α_1 is negative; the sum of α_0, α_1, and α_2 is also included, and is equal to one, as expected by Eq. (18) under $h = h_{max}$. For SLS glass, α_0 =

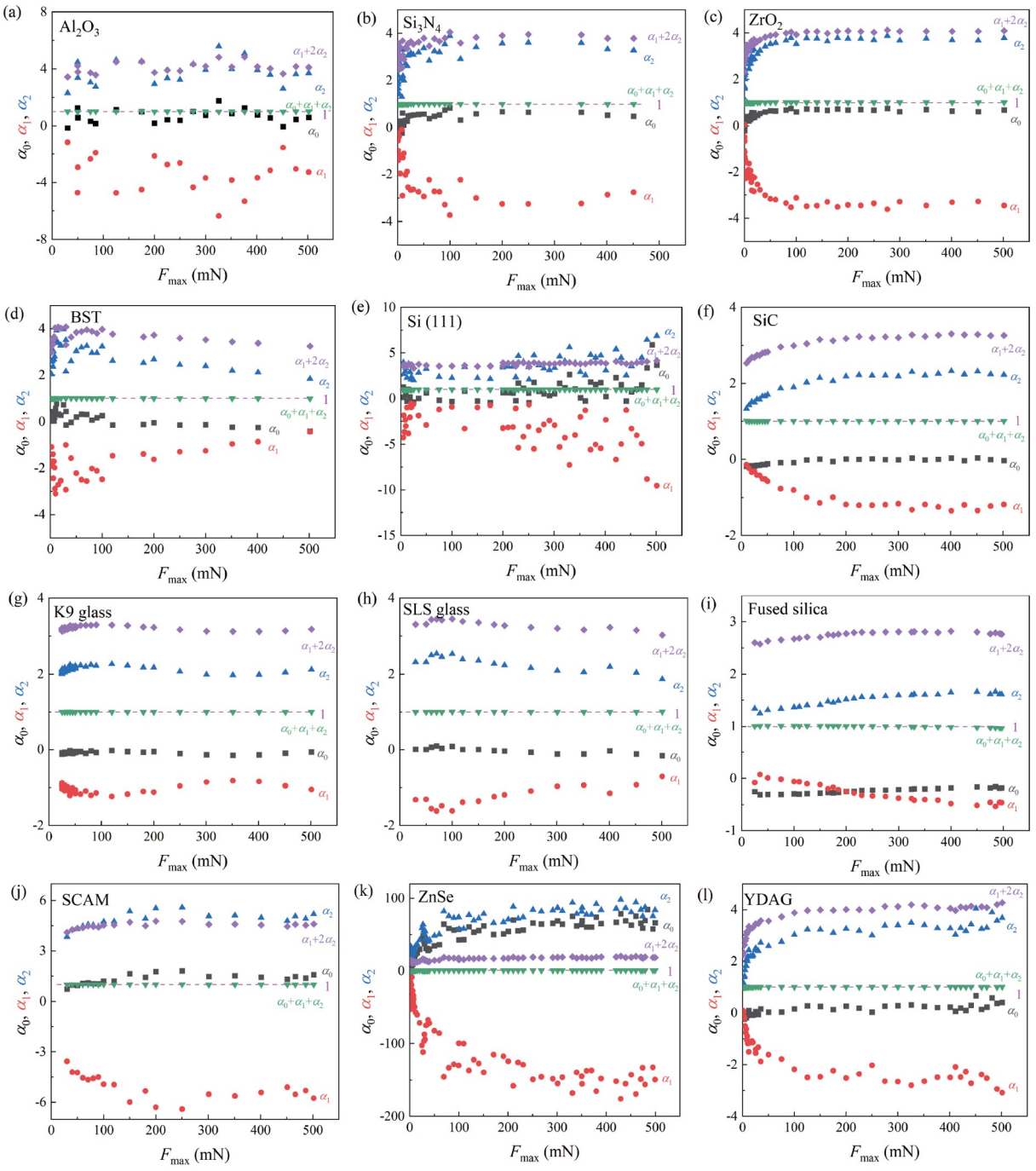

Figure 6 Variations of α_0, α_1, and α_2 in Eq. (18) with F_{max} for the 12 brittle solids. (a) Al_2O_3, (b) Si_3N_4, (c) ZrO_2, (d) BST, (e) Si (111), (f) SiC, (g) K9 glass, (h) SLS glass, (i) fused silica, (j) SCAM, (k) ZnSe, and (l) YDAG.

0.1, $\alpha_1 = -1.6$, $\alpha_2 = 2.6$, and $(\alpha_1 + 2\alpha_2) = 3.6$, which is almost the same as those reported in the previous study [120]. The large fluctuation of the three parameters α_0, α_1, and α_2 for Al_2O_3 in Fig. 6(a) and Si (111) in Fig. 6(e) is due to the defects of Al_2O_3 and phase transformation of Si, respectively; while $(\alpha_1 + 2\alpha_2)$ is less affected, and can be approximated to be constant under large loads. On the premise that α_1 and α_2 are constant and independent of load, continuous measurement of S can be obtained from F/h of the loading segment without the necessity of unloading. Assume a proportional relationship between contact stiffness S and the ratio of F/h during loading, see Fig. 3(j), contact stiffness S in Eqs. (17) and (33) can be replaced by that calculated by Eq. (18).

4.3 Elastic modulus by elastic recovery of Knoop imprint

Knoop indenter of elongated rhombohedral shape is more

suitable for investigating the micro-hardness of brittle material and films than Vickers and Berkovich indenters, since cracking is less likely to be induced under Knoop indenter that is more flattened and less sharp, and the maximum depth reached by Knoop indenter is 30% lower than that obtained by Vickers or Berkovich indenter under the same applied load [189,190]. Knoop hardness test can be used not only to measure fracture toughness of brittle ceramics by indentation-induced cracking [191-193], but also to calculate elastic modulus of various solids (e.g., polymer [194], ceramic [195], glass [196], optical crystal [197], coating [198]) based on elastic recovery [199,200].

Figure 7(a) shows the schematic diagram of the elastic recovery of Knoop indent after unloading: d and b are the long and short diagonals of residual Knoop indent, respectively; d' and b' are the long and short diagonals of Knoop indent, respectively, at full load ($b'/d' = 1/7.11$). After unloading, short diagonal decreases due to the elastic recovery (i.e., $b < b'$), and the decrease in the long diagonal is negligible (i.e., $d \approx d'$). Macroscopic elastic modulus E_K can be obtained based on the elastic recovery of Knoop indent [199]:

$$\frac{b}{d} = \frac{1}{7.11} - \alpha_K \frac{H_K}{E_K}, H_K = \frac{2P}{d^2} \cdot \frac{\tan\theta_1}{\tan\theta_2} = 14.229\frac{P}{d^2}, \tag{36}$$

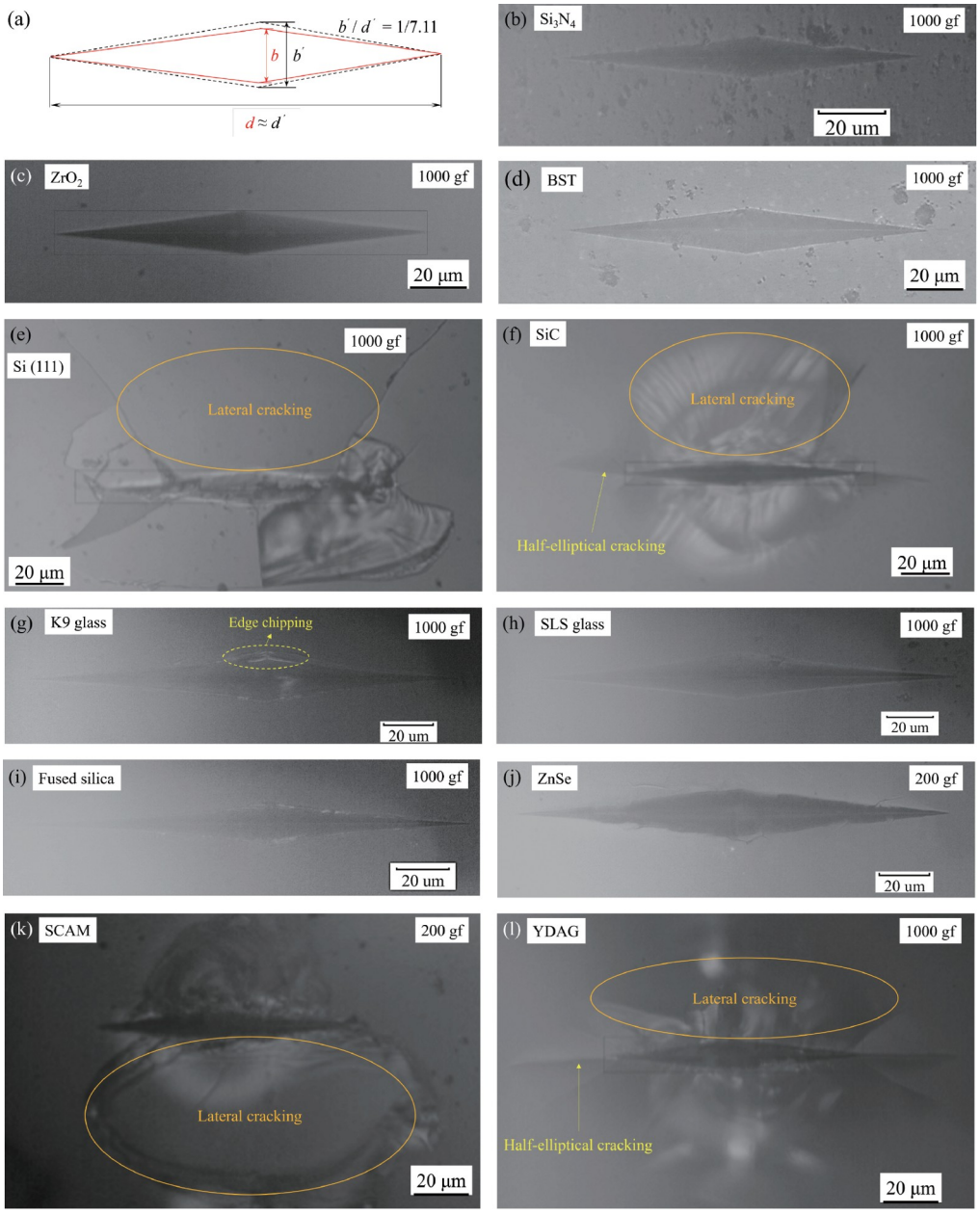

Figure 7 (a) Schematic diagram of the elastic recovery of Knoop indent after unloading; residual imprint of 11 brittle solids by Knoop indenter (P = 1000 gf for most materials, while P = 200 gf for SCAM and ZnSe): (b) Si_3N_4, (c) ZrO_2, (d) BST, (e) Si (111), (f) SiC, (g) K9 glass, (h) SLS glass, (i) fused silica, (j) ZnSe, (k) SCAM, and (l) YDAG.

where α_K is normally assumed to be a constant of 0.45 for ceramics [201], while is a linear function of b/d for bulk metallic glasses [202]; H_K is Knoop hardness, which is the mean pressure defined by the ratio of normal load P over the projected area of residual imprint created by the lozenge-based pyramid Knoop indenter [190], $\theta_1 = 86.25°$, and $\theta_2 = 65°$ are semi-apical angles of Knoop indenter, respectively. Reduced modulus E_r can be calculated by substituting E_K (i.e., E_{IT}) into Eq. (1).

Figure 7(b)-(l) show the residual imprints of 11 brittle solids (Al_2O_3 is not shown due to the invisible indents under optical microscopy) by Knoop indenter. No surface cracking is observed for ceramics, traditional glasses at load $P = 1000$ gf (1 gf = 9.81×10^{-3} N), and soft brittle ZnSe at load $P = 200$ gf; only imprints attributed to elastoplastic deformation can be observed, and similar phenomena can be found for ceramics Ref. [203]. Figure 7(e) and (k) show the surface uplifts due to the lateral cracking around the short diagonal of the Knoop indents of Si (111) and SCAM, respectively, in the absence of the half-elliptical cracking along the long diagonal, and the prominent surface uplifts are attributed to the cleavage characteristics and relatively low fracture toughness of material [204]. Figure 7(f) and (l) reveal that the half-elliptical cracks propagate along the long diagonal of the Knoop indents of SiC and YDAG, respectively, and half-elliptical cracks can intersect with the lateral cracks beneath the surface under large loads [191]. Only a little edge chipping can be observed for K9 glass by Knoop indenter under 9.8 N, as shown in Fig. 7(g), while surface radial cracking occurs under a smaller load of 0.5 N in nanoindentation by Berkovich indenter, see Fig. 2(g), which can be explained by noting that the blunter Knoop indenter of elongated rhombohedral shape is more flattened than Berkovich indenter, and is more suitable for investigating hardness of brittle solids than the sharper Vickers and Berkovich indenters. Moreover, under the same load $P = 1000$ gf, no surface cracking can be observed for BST ceramic and fused silica with Knoop indenter, while severe cracking damage can be found with a sharper Vickers indenter, as reported in Refs. [1,205]. Severe surface cracking/damage can be observed for semiconductors (i.e., Si and SiC), SCAM, and YDAG, which can be attributed to their single crystal microstructures, and ceramics of polycrystalline microstructures and glasses of non-crystal structure show excellent cracking resistance.

Figure 8(a) shows that b is proportional to d, and a constant value of b/d that is independent of load but dependent on material can be assumed. Only the materials under the appropriate loads with clearly visible b and in the absence of indentation-induced cracking are considered. The values of b/d of brittle solids are smaller than 1/7.11, indicating the decrease in short diagonal due to the elastic recovery, as expected, and the Knoop hardness, calculated based on the real residual Knoop imprint is smaller than that without considering the elastic recovery in short diagonal in Eq. (36). Figure 8(b) shows that the applied load P is proportional to d^2, and H_K can be calculated as a constant that is independent of load with the proportional coefficient.

4.4 Comparison of elastic modulus by different methods

Figure 9 compares reduced modulus E_r by different methods with E_r by OP method Eq. (1) as reference. Spearman rank correlation coefficient ρ is calculated as [206]

$$\rho = \frac{\sum_{i=1}^{N}(x_i-\bar{x})(y_i-\bar{y})}{\sqrt{\sum_{i=1}^{N}(x_i-\bar{x})^2\sum_{i=1}^{N}(y_i-\bar{y})^2}},$$
$$\bar{x} = \frac{\sum_{i=1}^{N}x_i}{N},\quad \bar{y} = \frac{\sum_{i=1}^{N}y_i}{N}, \tag{37}$$

where x and y represent the values obtained by OP method Eq. (1) and other methods (or in the literature), respectively; the subscript i is the serial number of E_r or H_{IT}; $N = 12$ is the total number of brittle solids; $\bar{x}$ and $\bar{y}$ are the arithmetic means of E_r (or H_{IT}) by OP method Eq. (1) and other methods, respectively.

Values of E_r in the literature and those calculated by

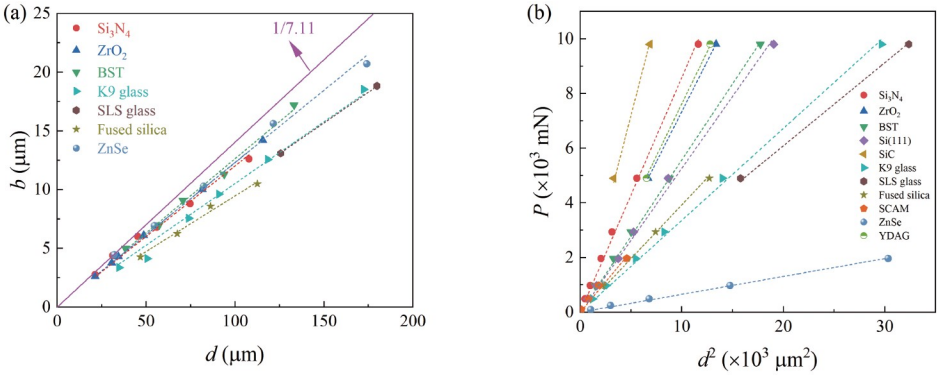

Figure 8 Proportional relationships between (a) b and d, and (b) P and d^2.

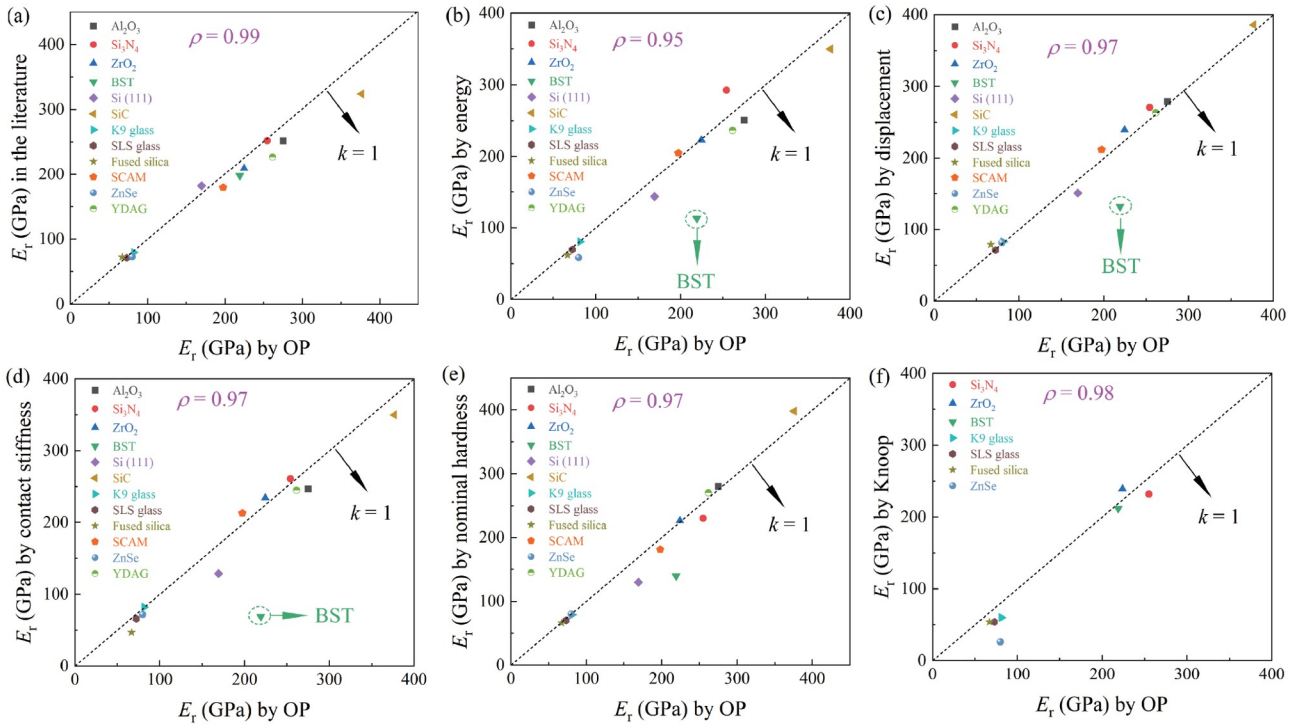

Figure 9 Comparison of E_r obtained by OP method Eq. (1) with those (a) in the literature, and calculated by (b) energy-based method Eq. (17), (c) displacement-based method Eq. (33), (d) contact stiffness-based method Eq. (20), (e) nominal hardness-based method Eq. (24), and (f) Knoop hardness-based method Eq. (36). ρ is the Spearman rank correlation coefficient calculated by Eq. (37), and the data for BST circled by dotted lines were discarded when calculating ρ.

various methods are almost the same, and the values of ρ between E_r calculated by various methods and those by OP method Eq. (1) are not smaller than 0.95, indicating that elastic modulus of brittle solids can be characterized by various methods such as energy-based method Eq. (17), displacement-based method Eq. (33), contact stiffness-based method Eq. (20), nominal hardness-based method Eq. (24), and Knoop hardness-based method Eq. (36). Values of E_r of BST obtained by energy-based, displacement-based, and contact stiffness-based methods are much smaller than that obtained by OP method, see Fig. 9(b)-(d), which can be explained by noting the inhomogeneity and defects of BST ceramic. Only the materials without indentation-induced cracking are considered in Fig. 9(f). Knoop hardness-based method Eq. (36) is an easy and suitable method to obtain E_r of brittle solids in the absence of indentation-induced cracking [191-193].

4.5 Hardness analysis

Figure 10(a) and (b) shows the variations of projected contact area A_p, which is calculated by contact stiffness-based method Eq. (20) with the fitting parameters, see Fig. 3(o), and A_{max}, which is calculated by $A_{max} = 24.5(h_{max} + \Delta h)^2$ in Eq. (23) with Δh, see Fig. 1, with F_{max}. Proportional relationships can be normally assumed between F_{max} and A_p, and F_{max} and A_{max}, with their proportionalities being the indentation hardness H_{IT} (= F_{max}/A_p) and nominal hardness H_n (= F_{max}/A_{max}), respectively, which can be regarded to be constant and independent of load. For BST, the proportional relationship between A_p and F_{max} holds under small loads, the relationship between A_p and F_{max} becomes nonlinear under large loads, which might be attributed to the defects and inhomogeneity of the newly prepared ceramic by sintering. For fused silica, the relationship between A_{max} and F_{max} under large loads deviates from the proportional relationship under small loads, which is mainly attributed to the indentation-induced cracking under large loads. Figure 10(c) compares the contact protected area A_p by contact stiffness-based method Eq. (20) and the maximum projected area A_{max} by Eq. (23), and values of A_p are normally smaller than those of A_{max}, and linear relationship can be approximated. For BST, A_p is larger than A_{max} with a nonlinear relationship, which can be attributed to the dielectric characteristic of BST. For fused silica, A_p is larger than A_{max} under small loads, while A_p is smaller than A_{max} under large loads due to indentation-induced cracking. For ZnSe, A_p and A_{max}, which are much larger than those of other materials, are more or less the same, which is attributed to its excellent ductility. Fused silica is a standard material used for calibration of area function of the indenter, and the applied should not exceed 100 mN to prevent indentation-induced cracking, resulting in a relatively small range of contact

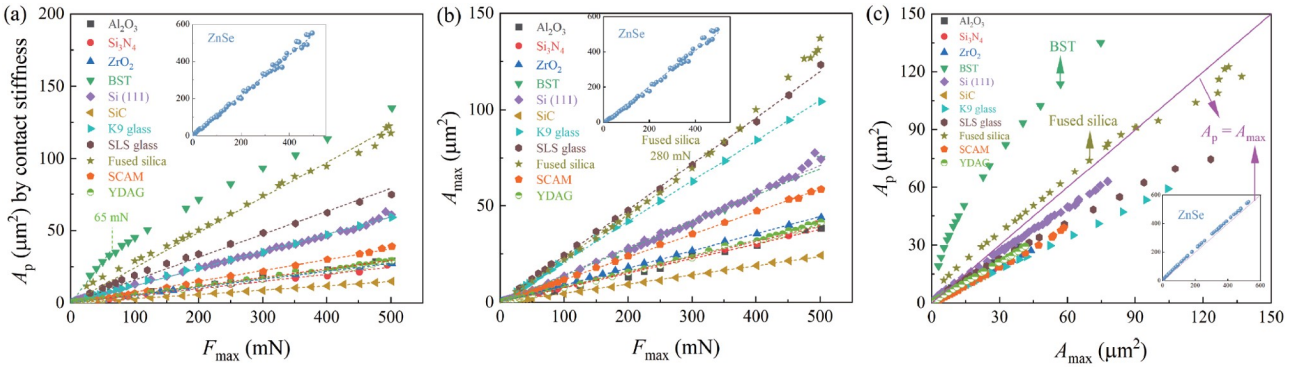

Figure 10 Variation of (a) the contact protected area A_p by contact stiffness-based method Eq. (21), and (b) the maximum projected area A_{max} by Eq. (23) with F_{max} (the proportional relationship for fused silica holds under small loads); (c) comparison between A_p and A_{max}.

depth that is calibrated. ZnSe is believed to be more suitable than fused silica for calibration of the indenter, since the calibrated range of contact depth would become much larger than that by fused silica.

Figure 11(a)-(e) compare indentation hardness by different methods with H_{IT} by OP method Eq. (1) as reference. Values of H_{IT} in the literature and those obtained by OP method Eq. (1), energy-based method Eq. (17), and displacement-based method Eq. (33) are almost the same. H_{IT} of SiC obtained by OP method Eq. (1) is much larger than that in Ref. [128], which can be explained by noting that the loads used in the current work are smaller than those used for micro-hardness tests [128], and the smaller hardness reported in the literature is due to the indentation-induced cracking under large loads in micro-hardness tests.

Figure 11(d) shows that values of H_{IT} obtained by contact stiffness-based method Eq. (21) is proportional to those obtained by OP method Eq. (1) with the proportionality being 0.8 and smaller than 1, and A_p calculated by Eq. (20) is larger than that by OP method, which can be explained by noting that a simple quadratic polynomial function without the constant term is used to relate S^2 and h_c. Figure 11(e) shows that values of nominal hardness H_n by Eq. (22) are proportional to those of H_{IT} by OP method Eq. (1) with the proportional coefficient being 0.6 and smaller than 1, since A_{max} is larger than A_p under the same load. Figure 11(f)

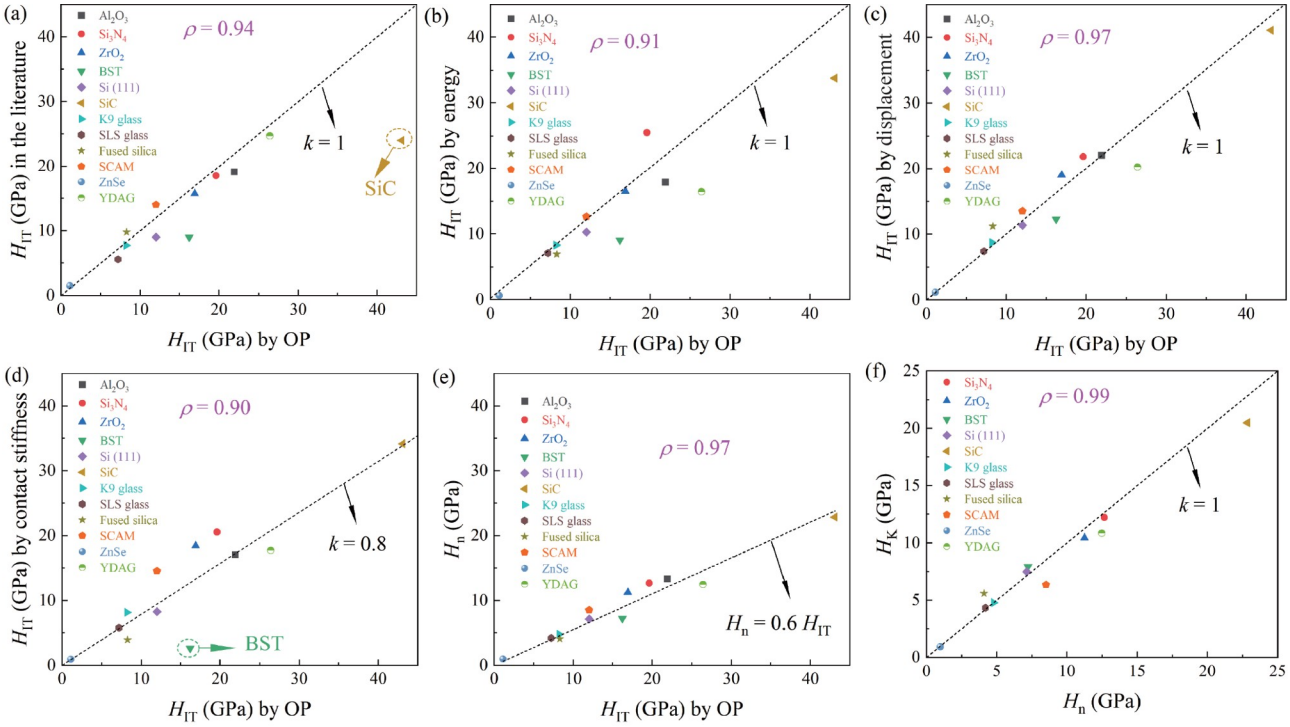

Figure 11 Comparison of H_{IT} obtained by OP method Eq. (1) with those (a) in the literature, and calculated by (b) energy-based method Eq. (17), (c) displacment-based method Eq. (33), (d) contact stiffness-based method Eq. (21), (e) nominal hardness H_n (22); (f) comparison between H_n by Eq. (22) and Knoop hardness H_K by Eq. (36). ρ represents the Spearman rank correlation coefficient calculated by Eq. (37).

shows that values of Knoop hardness H_K by Eq. (36) are almost the same as those of H_n by Eq. (22), demonstrating the equivalence between the nominal hardness calculated based on the maximum displacement during nanoindentation by Berkovich indenter and the micro-hardness by Knoop indenter. The values of ρ are larger than 0.9 in Fig. 11, indicating that indentation hardness H_{IT} of brittle solids can be characterized by different methods, and displacement-based method Eq. (33) with the largest ρ is believed to be the most suitable method to obtain indentation hardness without the need of area function of the indenter.

Figure 12(a) and (b) shows the dependence of H_p calculated by Eq. (28) with E^* rather than E_r on H_{IT} and E^* obtained by OP method, respectively. Figure 12(c) and (d) shows the dependence of H_p calculated by Eq. (28) with E_r rather than E^* on H_{IT} and E_r obtained by OP method, respectively. For most materials expect the three traditional glasses: power law function can be used to relate H_p calculated by E^* with H_{IT}; H_p calculated by E^* is proportional to the square root of E^* by OP method; H_p calculated by E_r is proportional to the square root of H_{IT}; and H_p calculated by E_r is proportional to E_r. The particular behavior of the three traditional glasses distinguishing from other materials can be explained by noting the small recovery resistance R_s shown in Fig. 3(k), which is attributed to homogeneity and isotropy of the amorphous glasses [54,205], and other materials are crystalline, indicating the special deformation mechanism (e.g., densification without dislocation) of amorphous glasses. Figure 12(e) shows that H_p calculated by E^* is proportional to that calculated by E_r with proportional coefficient of 0.93, indicating the significant role of elastic deformation of the indenter. Only SiC deviates far from the predicted line, which can be explained by noting that both H_{IT} and E_r of SiC are much larger than those of other materials. Figure 12(f) shows that H_{IT} and E_r obtained by OP method Eq. (1) are linearly correlated, which has been widely reported for brittle materials (e.g., YAG single crystals [207], covalent materials [208], and transition metal diborides [209]), since indentation hardness, which is an important parameter for the assessment of plasticity, is directly related to the reduced modulus in a linear/quadratic way [104]. The three traditional glasses and SiC do not follow the predicted line, which can be explained by noting the small recovery resistance of the three traditional glasses, as shown in Fig. 3(k), and both large hardness and modulus of SiC, as shown in Table 3.

5. Conclusions

Reduced elastic modulus E_r and indentation hardness H_{IT} of the brittle solids such as ceramics, semiconductors, glasses, single crystals, and laser material, were characterized by instrumented indentation with Berkovich indenter, and mi-

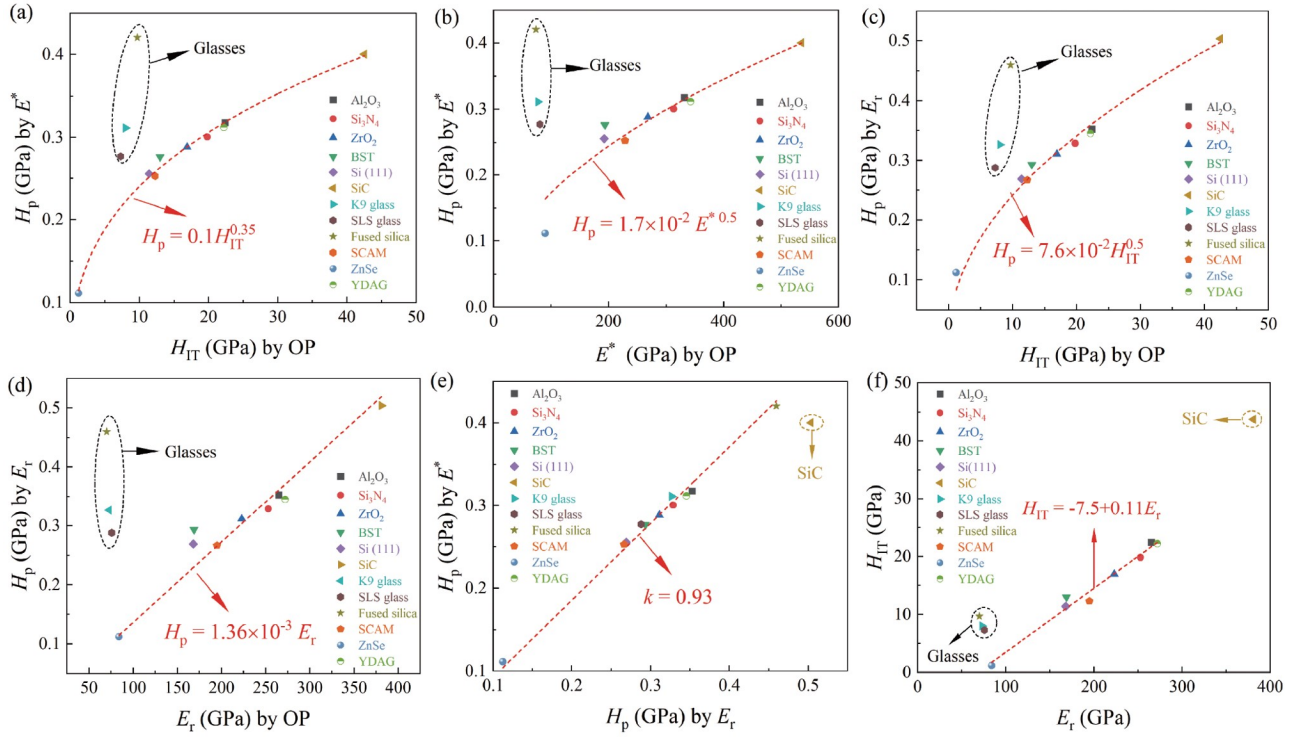

Figure 12 Relationships between H_p calculated based on E^* and (a) H_{IT} by OP method, and (b) E^* by OP method. Relationships between H_p calculated based on E_r and (c) H_{IT}, and (d) E_r by OP method. Relationships between hardness and elastic modulus: (e) H_p calculated by E^* vs. H_p calculated by E_r, and (f) H_{IT} vs. E_r.

cro-hardness with Knoop indenter. Nonlinear rather than linear expressions are found to be applicable to relate H_{IT}/E_r to W_e/W_t and h_p/h_{max}. E_r and H_{IT} can be obtained from various methods such as energy-based, displacement-based, and contact stiffness-based methods without the need of area function of the indenter. Knoop hardness-based method provides an easy approach of measuring elastic modulus of brittle solids in the absence of cracking. Elastic modulus can be characterized based on the elastic recovery of the imprint by Knoop indenter Eq. (36) under the appropriate loads with clearly visible short diagonal and little indentation-induced damage. Values of indentation hardness of brittle solids by displacement-based method are most consistent with those by OP method. Knoop hardness is found to be equivalent to nominal hardness calculated by the maximum indentation displacement. Plastic hardness H_p on the basis of E_r is found to be proportional to $E_r\sqrt{H_{IT}}$ for brittle solids except for traditional glasses.

Conflict of interest *On behalf of all authors, the corresponding author states that there is no conflict of interest.*

Author contributions ***Zhitong Xu:*** *Investigation, Formal analysis, Validation, Visualization, Methodology, Data curation, Writing – original draft, Writing – review & editing.* ***Ming Liu:*** *Methodology, Supervision, Validation, Visualization, Conceptualization, Writing – review & editing, Funding acquisition, Resources, Project administration.* ***Jianghong Gong:*** *Methodology, Supervision, Visualization, Writing – review & editing.*

Acknowledgements *This work was supported by the National Natural Science Foundation of China (Grant No. 51705082), Fujian Provincial Minjiang Scholar Program (Grant No. 0020-510759), Qishan Sholar program in Fuzhou University (Grant No. 0020-650289), and Fuzhou University Testing Fund of precious apparatus (Grant No. 2023T018).*

1 M. Liu, and Z. Xu, Micromechanical characterization of microwave dielectric ceramic BaO-Sm_2O_3-5TiO_2 by indentation and scratch methods, J. Adv. Ceram. **12**, 1136 (2023).
2 Z. Wang, Z. Dong, Y. Ran, R. Kang, and Y. Bao, On understanding the mechanical properties and damage behavior of Cf/SiC composites by indentation method, J. Mater. Res. Tech. **26**, 3784 (2023).
3 Z. Xu, M. Liu, and F. Yang, Calculation of elastic constants of bulk metallic glasses from indentation tests, J. Mater. Res. Tech. **28**, 4382 (2024).
4 X. Long, S. Wang, Y. Feng, Y. Yao, and L. M. Keer, Annealing effect on residual stress of Sn-3.0Ag-0.5Cu solder measured by nanoindentation and constitutive experiments, Mater. Sci. Eng.-A **696**, 90 (2017).
5 Z. Yu, and Y. Wei, Cross-scale indentation scaling relationships of strain gradient plastic solids: Influence of inclusions near the indenter tip, Acta Mech. Sin. **38**, 221257 (2022).
6 H. Xiang, and W. Guo, A newly developed interatomic potential of Nb-Al-Ti ternary systems for high-temperature applications, Acta Mech. Sin. **38**, 121451 (2022).
7 D. Fang, W. Li, T. Cheng, Z. Qu, Y. Chen, R. Wang, and S. Ai, Review on mechanics of ultra-high-temperature materials, Acta Mech. Sin. **37**, 1347 (2021).
8 J. Zhu, M. Wei, J. Xu, R. Yang, X. Meng, P. Zhang, J. Yang, G. Li, and F. Gao, Influence of order-disorder transition on the mechanical and thermophysical properties of $A_2B_2O_7$ high-entropy ceramics, J. Adv. Ceram. **11**, 1222 (2022).
9 P. Galizia, S. Failla, C. Melandri, and D. Sciti, Local indentation response of carbon fibers embedded in a harsh environment: The sintered ultra-high temperature ceramic matrix, J. Eur. Ceram. Soc. **44**, 5347 (2023).
10 J. Devillard, J. Adrien, S. Roux, S. Meille, and E. Maire, Highlighting the role of heterogeneity on the indentation hardness of foamed gypsum, J. Eur. Ceram. Soc. **40**, 3795 (2020).
11 F. Z. Y. Huang, The indenter tip radius effect in micro- and nanoindentation hardness experiments, Acta Mech. Sin. **22**, 1 (2006).
12 X. Zhou, L. Liu, J. Sun, N. Zhang, H. Sun, H. Wu, and W. Tao, Effects of $(Mg_{1/3}Sb_{2/3})^{4+}$ substitution on the structure and microwave dielectric properties of $Ce_2Zr_3(MoO_4)_9$ ceramics, J. Adv. Ceram. **10**, 778 (2021).
13 C. Feng, X. Zhou, B. Tao, H. Wu, and S. Huang, Crystal structure and enhanced microwave dielectric properties of the $Ce_2[Zr_{1-x}(Al_{1/2}Ta_{1/2})_x]_3(MoO_4)_9$ ceramics at microwave frequency, J. Adv. Ceram. **11**, 392 (2022).
14 D. Hou, M. Liu, S. Liu, and F. Yang, Indentation fracture of 4H-SiC single crystal, Int. J. Mech. Sci. **270**, 109096 (2024).
15 R. Li, Y. Li, C. Yan, Y. Bao, H. Sun, H. Hu, and N. Li, Thickness-dependent and tunable mechanical properties of $CaTiO_3$ dielectric thin films determined by nanoindentation technique, Ceram. Int. **46**, 22643 (2020).
16 A. Moradkhani, H. Baharvandi, M. Tajdari, H. Latifi, and J. Martikainen, Determination of fracture toughness using the area of micro-crack tracks left in brittle materials by Vickers indentation test, J. Adv. Ceram. **2**, 87 (2013).
17 X. Zhang, K. Zhang, B. Zhang, Y. Li, and R. He, Mechanical properties of additively-manufactured cellular ceramic structures: A comprehensive study, J. Adv. Ceram. **11**, 1918 (2022).
18 S. Fan, T. Sun, M. Jiang, S. Gu, L. Wang, H. Yan, and W. Jiang, In-situ growth of carbon nanotubes on ZnO to enhance thermoelectric and mechanical properties, J. Adv. Ceram. **11**, 1932 (2022).
19 C. D. Rivera-Tello, F. J. Flores-Ruiz, M. Flores-Jiménez, and M. Flores, Influence of plasma ionization on the elastic modulus and tribology behavior of carbon films deposited by the HiPIMS technique, Ceram. Int. **49**, 2427 (2023).
20 Y. Xiao, J. Wu, H. Shen, X. Hu, and H. Yong, Damage behavior in Bi-2212 round wire with 3D elastoplastic peridynamic, Acta Mech. Sin. **39**, 422431 (2023).
21 Z. Du, Y. Yang, Z. Wang, X. Fan, and T. Lu, A finite strain visco-hyperelastic damage model for rubber-like materials: theory and numerical implementation, Acta Mech. Sin. **39**, 222473 (2023).
22 B. H. Sun, Small symmetrical deformation and stress analysis of catenary shells of revolution, Acta Mech. Sin. **38**, 421425 (2022).
23 D. Wang, Z. Zhang, Z. B. Li, Q. Wang, B. Qiu, Q. Han, and W. You, Prediction of macroscopic effective elastic modulus of micro-nano-composite ceramic tool materials based on microstructure model, Ceram. Int. **48**, 18558 (2022).
24 M. Z. Ibrahim, A. A. D. Sarhan, F. Yusuf, and M. Hamdi, Biomedical materials and techniques to improve the tribological, mechanical and biomedical properties of orthopedic implants—A review article, J. Alloys Compd. **714**, 636 (2017).
25 V. P. Ricci, C. R. M. Afonso, R. F. M. dos Santos, A. M. Jorge Junior, and V. Roche, Anodic growth and pre-calcification on β-Ti-40Nb alloy: Effects on elastic modulus, electrochemical properties, and bioactivity, Ceram. Int. **48**, 27575 (2022).
26 B. R. Lawn, and D. B. Marshall, Hardness, toughness, and brittleness: An indentation analysis, J. Am. Ceram. Soc. **62**, 347 (1979).
27 B. J. Zadler, J. H. L. Le Rousseau, J. A. Scales, and M. L. Smith, Resonant ultrasound spectroscopy: Theory and application, Geophys. J. Int. **156**, 154 (2004).
28 C. Bi, G. H. Tang, C. B. He, X. Yang, and Y. Lu, Elastic modulus prediction based on thermal conductivity for silica aerogels and fiber reinforced composites, Ceram. Int. **48**, 6691 (2022).
29 H. Cai, F. Guo, Z. Zhang, X. Shan, X. Wang, X. Fan, and X. Zhao, Flexural strength and elastic modulus of gradient structured YSZ

membranes with multi-scale pores, Ceram. Int. **48**, 27931 (2022).
30 C. Lee, X. Wei, J. W. Kysar, and J. Hone, Measurement of the elastic properties and intrinsic strength of monolayer graphene, Science **321**, 385 (2008).
31 J. Zhang, C. Zhang, S. Mu, S. Wang, and H. Li, Characterization of mechanical properties of in-service nickel-based alloy by continuous indentation, Structures **48**, 1346 (2023).
32 T. Ishibashi, S. Shimoda, T. Furukawa, I. Nitta, and H. Yoshida, The measuring method about Young's modulus of plastics using the indenting hardness test by a spherical indenter, Trans. Jpn. Soc. Mech. Eng. **53**, 2193 (1987).
33 A. Naughton Duszová, L. Ďaková, T. Csanádi, A. Kovalčíková, V. Kombamuthu, H. Ünsal, P. Tatarko, M. Tatarková, P. Hvizdoš, and P. Šajgalík, Nanohardness and indentation fracture resistance of dual-phase high-entropy ceramic, Ceram. Int. **49**, 24239 (2023).
34 A. Orozco-Caballero, C. Gutierrez, B. Gan, and J. M. Molina-Aldareguia, High-throughput nanoindentation mapping of cast IN718 nickel-based superalloys: Influence of the Nb concentration, J. Mater. Res. **36**, 2213 (2021).
35 H. Fu, L. Cai, Z. Chai, X. Liu, L. Zhang, S. Geng, K. Zhang, H. Liao, X. Wu, X. Wang, D. Liu, and J. Chen, Evaluation of bonding properties by flat indentation method for an EBW joint of RAFM steel for fusion application, Nucl. Mater. Energy **25**, 100861 (2020).
36 M. Liu, and F. Yang, Indentation-induced interface decohesion between a piezoelectric film and an elastic substrate, J. Comp. Theo. Nano. **11**, 1863 (2014).
37 M. Liu, and F. Yang, Finite element analysis of the indentation-induced delamination of bi-layer structures, J. Comp. Theo. Nano. **9**, 851 (2012).
38 H. Chen, L. Cai, and C. Bao, Equivalent-energy indentation method to predict the tensile properties of light alloys, Mater. Des. **162**, 322 (2019).
39 H. M. Sajjad, H. ul Hassan, M. Kuntz, B. J. Schäfer, P. Sonnweber-Ribic, and A. Hartmaier, Inverse method to determine fatigue properties of materials by combining cyclic indentation and numerical simulation, Materials **13**, 3126 (2020).
40 Z. Zhang, M. Liu, H. Tu, Z. Ba, B. Zhang, and Z. Hu, Nanoindentation creep behaviour and microstructural evolution of long-term crept HR3C austenitic steel, Mater. High Temp. **38**, 403 (2021).
41 H. R. Xiao, L. X. Cai, and G. Z. Han, Semi-analytical creep model to obtain Norton's law of materials under flat indentation and its applications, J. Mater. Res. Tech. **25**, 905 (2023).
42 M. Liu, Z. T. Xu, and F. Q. Yang, Characterization of cyclic dynamic and creep responses of pure aluminum by instrumented indentation, Sci. Sin.-Phys. Mech. Astron. **53**, 214605 (2023).
43 D. Chicot, F. Roudet, V. Lepingle, and G. Louis, Strain gradient plasticity to study hardness behavior of magnetite (Fe_3O_4) under multicyclic indentation, J. Mater. Res. **24**, 749 (2009).
44 K. Yu, J. Cheng, Q. Cheng, Y. Geng, S. Zhu, M. Liu, S. Wan, and J. Yang, Enhanced wear resistance in $(CoCrNi)_{94}Al_3Ti_3$ medium-entropy alloy at high temperatures via nano-Al_2O_3 reinforcing phase, Tribol. Int. **195**, 109569 (2024).
45 Y. Li, D. Omacht, F. Yu, and M. Sun, A new spherical indentation approach to determine fracture toughness of high strength steels, Eng. Fract. Mech. **272**, 108695 (2022).
46 H. Yin, S. Wang, Q. Zhao, J. Zhang, X. Mao, and B. Guo, Surface fracture behavior and subsurface damage of polycrystalline yttrium aluminum garnet ceramics in Vickers indentation, J. Mater. Res. Tech. **26**, 5975 (2023).
47 D. Chicot, F. Roudet, A. Zaoui, G. Louis, and V. Lepingle, Influence of visco-elasto-plastic properties of magnetite on the elastic modulus: Multicyclic indentation and theoretical studies, Mater. Chem. Phys. **119**, 75 (2010).
48 Y. Chen, S. Qiu, Z. He, F. Yan, R. Li, and Y. Feng, Comparative analysis of indentation and magnetic resonance elastography for measuring viscoelastic properties, Acta Mech. Sin. **37**, 527 (2021).
49 J. J. Roa, I. Sapezanskaia, G. Fargas, R. Kouitat, A. Redjaïmia, and A. M. Mateo, Reversible phase transformation in polycrystalline TRIP steels induced by cyclic indentation performed at the nanometric length scale, Steel Res. Int. **89**, 1800234 (2018).
50 M. Skrzypczak, C. Guerret-Piecourt, S. Bec, J. L. Loubet, and O. Guerret, Use of a nanoindentation fatigue test to characterize the ductile-brittle transition, J. Eur. Ceram. Soc. **29**, 1021 (2009).
51 Y. Takagawa, M. Nakamura, K. Miura, and J. Kobata, Relationships between Raman parameters obtained from cyclic indentation impressions on DLC coatings, Surf. Interface Anal. **52**, 859 (2020).
52 H. Toyama, H. Kishida, and A. Yonezu, Characterization of fatigue crack growth of concrete mortar under cyclic indentation loading, Eng. Fail. Anal. **83**, 156 (2018).
53 M. M. Islam, S. I. Shakil, N. M. Shaheen, P. Bayati, and M. Haghshenas, An overview of microscale indentation fatigue: Composites, thin films, coatings, and ceramics, Micron **148**, 103110 (2021).
54 C. Gao, and M. Liu, Characterization of spherical indenter with fused silica under small deformation by Hertzian relation and Oliver and Pharr's method, Vacuum **153**, 82 (2018).
55 Z. Li, K. F. Wang, B. L. Wang, and J. E. Li, Size effect on the punch performance of brittle porous ceramics: Theoretical analysis and numerical simulation, Int. J. Mech. Sci. **207**, 106674 (2021).
56 M. Liu, D. Hou, and C. Gao, Berkovich nanoindentation of $Zr_{55}Cu_{30}Al_{10}Ni_5$ bulk metallic glass at a constant loading rate, J. Non-Cryst. Solids **561**, 120750 (2021).
57 M. Liu, Z. Xu, and H. Wei, Characterization of elastic modulus and yield strength of metals by Knoop hardness (in Chinese), J. Harbin Inst. Technol. **56**, 108 (2024).
58 Y. Chen, and L. Dai, Failure behavior and criteria of metallic glasses, Acta Mech. Sin. **38**, 121449 (2022).
59 Z. Xiong, P. Tao, Z. Long, Z. Huang, K. Long, X. Zhu, X. Xu, H. Deng, H. Lin, and W. Li, The effect of Ta addition on mechanical properties of Zr-based bulk metallic glasses, Intermetallics **153**, 107779 (2023).
60 G. Zhao, M. Liu, and F. Yang, The effect of an electric current on the nanoindentation behavior of tin, Acta Mater. **60**, 3773 (2012).
61 M. Liu, Z. Xu, and C. Gao, Determination of mechanical properties of microstructure in metals based on grid nanoindentation, J. Fuzhou Univ. (Nat. Sci. Ed.) **49**, 797 (2021).
62 H. Chen, H. Peng, L. Cai, Z. Meng, W. Li, Z. Fu, and Z. Shen, A novel combined dual-conical indentation model for determining plastic properties of metallic materials, J. Mater. Res. Tech. **20**, 3241 (2022).
63 X. Long, Z. Shen, J. Li, R. Dong, M. Liu, Y. Su, and C. Chen, Size effect of nickel-based single crystal superalloy revealed by nanoindentation with low strain rates, J. Mater. Res. Tech. **29**, 2437 (2024).
64 X. Long, Q. P. Jia, Z. Li, and S. X. Wen, Reverse analysis of constitutive properties of sintered silver particles from nanoindentations, Int. J. Solids Struct. **191-192**, 351 (2020).
65 X. Long, B. Hu, Y. Feng, C. Chang, and M. Li, Correlation of microstructure and constitutive behaviour of sintered silver particles via nanoindentation, Int. J. Mech. Sci. **161-162**, 105020 (2019).
66 H. Chen, L. Cai, and C. Li, An elastic-plastic indentation model for different geometric indenters and its applications, Mater. Today Commun. **25**, 101440 (2020).
67 H. Li, J. Chen, Q. Chen, and M. Liu, Determining the constitutive behavior of nonlinear visco-elastic-plastic PMMA thin films using nanoindentation and finite element simulation, Mater. Des. **197**, 109239 (2021).
68 S. Park, K. P. Marimuthu, G. Han, and H. Lee, Deep learning based nanoindentation method for evaluating mechanical properties of polymers, Int. J. Mech. Sci. **246**, 108162 (2023).
69 C. Fan, K. Liu, Y. Wang, L. Zhang, and L. Sun, Nano-indentation and nano-scratch of flexible intraocular lens material at the molecular scale, Acta Mech. Sin. **39**, 122331 (2023).

70 X. Liu, L. Cai, H. Chen, and S. Si, Semi-analytical model for flat indentation of metal materials and its applications, Chin. J. Aeronaut. **33**, 3266 (2020).
71 M. Liu, and F. Yang, Three-dimensional finite element simulation of the Berkovich indentation of a transversely isotropic piezoelectric material: Effect of material orientation, Model. Simul. Mater. Sci. Eng. **21**, 045014 (2013).
72 M. Liu, and F. Yang, Orientation effect on the Boussinesq indentation of a transversely isotropic piezoelectric material, Int. J. Solids Struct. **50**, 2542 (2013).
73 G. Wu, M. Gotthardt, and M. Gollasch, Assessment of nanoindentation in stiffness measurement of soft biomaterials: Kidney, liver, spleen and uterus, Sci. Rep. **10**, 18784 (2020).
74 L. Angker, M. V. Swain, and N. Kilpatrick, Characterising the micro-mechanical behaviour of the carious dentine of primary teeth using nano-indentation, J. Biomech. **38**, 1535 (2005).
75 M. Liu, and F. Yang, Finite element simulation of the effect of electric boundary conditions on the spherical indentation of transversely isotropic piezoelectric films, Smart Mater. Struct. **21**, 105020 (2012).
76 M. Liu, Finite element analysis of effects of mechanical properties on indentation-induced interfacial delamination, J. Comp. Theo. Nano. **11**, 1697 (2014).
77 P. Dziarski, and N. Makuch, Effect of indentation load on nanomechanical properties measured in a multiphase boride layer, Materials **14**, 6727 (2021).
78 Y. Li, H. Zhang, X. Li, P. Shi, X. Feng, and S. Ding, Surface effects on the indentation of a soft layer on a rigid substrate with an elliptical cylinder indenter, Acta Mech. Sin. **38**, 422098 (2022).
79 J. Zhou, D. Li, J. Zhang, and Z. Zhong, Interphase mechanical behaviors of nickel/yttria-stabilized zirconia cermets: A study by nanoindentation and molecular dynamics simulations, Int. J. Mech. Sci. **237**, 107791 (2023).
80 Q. Lü, S. Liu, W. Mao, Y. Yu, and X. Long, A numerical simulation-based ANN method to determine the shear strength parameters of rock minerals in nanoscale, Comput. Geotech. **169**, 106175 (2024).
81 K. Zheng, Y. Lin, T. Lai, C. Gao, M. Liu, and Z. Ren, Replacing copper in composites with waste foundry sand: A novel approach for Cu-free resin-based braking material, Tribol. Int. **191**, 109110 (2024).
82 C. Zhang, Y. Li, and H. Zhao, Mechanical contribution of the pia-arachnoid complex to brain tissue revealed by large deformation indentation, Acta Mech. Sin. **40**, 623306 (2024).
83 Z. Yang, J. Gao, L. Duan, M. Luo, F. Yu, R. Xu, M. Zhou, F. R. Tay, L. Niu, W. Zhou, and J. Chen, Evaluation of a novel primer containing isocyanate group on dentin bonding durability, Dent. Mater. **39**, 455 (2023).
84 M. Bentoumi, E. H. Raouache, Z. Driss, A. Montagne, A. Iost, A. Mejias, and D. Chicot, Multicyclic indentation on brittle glasses, Ceram. Int. **47**, 26168 (2021).
85 Q. Kang, X. Fang, C. Wu, P. Verma, H. Sun, B. Tian, L. Zhao, S. Wang, N. Zhu, R. Maeda, and Z. Jiang, Mechanical properties and indentation-induced phase transformation in 4H-SiC implanted by hydrogen ions, Ceram. Int. **48**, 15334 (2022).
86 Y. Li, X. Fang, E. Tochigi, Y. Oshima, S. Hoshino, T. Tanaka, H. Oguri, S. Ogata, Y. Ikuhara, K. Matsunaga, and A. Nakamura, Shedding new light on the dislocation-mediated plasticity in wurtzite ZnO single crystals by photoindentation, J. Mater. Sci. Tech. **156**, 206 (2023).
87 M. A. Mazo, D. Soriano, and J. Rubio, Mechanical response of silicon oxycarbide materials processed by spark plasma sintering, Ceram. Int. **49**, 12866 (2023).
88 K. Lu, Q. He, J. Xie, H. Yang, Z. Chen, D. Ge, C. Zhou, and L. Yin, Nano-to-microscale ductile-to-brittle transitions for edge cracking suppression in single-diamond grinding of lithium metasilicate/disilicate glass-ceramics, J. Eur. Ceram. Soc. **43**, 1698 (2023).
89 Y. Chen, A. Zhang, and B. C. Prorok, Optimizing the indirect indentation method for brittle material property measurements, Ceram. Int. **47**, 9635 (2021).
90 W. J. Zong, D. Wu, and C. L. He, Radius and angle determination of diamond Berkovich indenter, Measurement **104**, 243 (2017).
91 Y. Choi, H. S. Lee, and D. Kwon, Analysis of sharp-tip-indentation load-depth curve for contact area determination taking into account pile-up and sink-in effects, J. Mater. Res. **19**, 3307 (2004).
92 X. Xiao, S. Li, and L. Yu, Effect of irradiation damage and indenter radius on pop-in and indentation stress-strain relations: Crystal plasticity finite element simulation, Int. J. Mech. Sci. **199**, 106430 (2021).
93 A. Greco, E. Sgambitterra, and F. Furgiuele, A new methodology for measuring residual stress using a modified Berkovich nano-indenter, Int. J. Mech. Sci. **207**, 106662 (2021).
94 A. A. Abubakar, A. Y. Adesina, A. F. M. Arif, J. Albinmousa, K. S. Al-Athel, and S. S. Akhtar, Evaluation of residual stress in thick metallic coatings using the combination of hole drilling and micro-indentation methods, J. Mater. Res. Tech. **20**, 867 (2022).
95 Z. Shen, R. Dong, J. Li, Y. Su, and X. Long, Determination of gradient residual stress for elastoplastic materials by nanoindentation, J. Manuf. Process. **109**, 359 (2024).
96 T. Y. Zhang, and W. H. Xu, Surface effects on nanoindentation, J. Mater. Res. **17**, 1715 (2002).
97 M. Mata, and J. Alcalá, The role of friction on sharp indentation, J. Mech. Phys. Solids **52**, 145 (2004).
98 W. Zhou, and F. Yang, Effects of surface stress on the indentation response of an elastic half-space, Int. J. Mech. Sci. **229**, 107512 (2022).
99 A. J. Moseson, S. Basu, and M. W. Barsoum, Determination of the effective zero point of contact for spherical nanoindentation, J. Mater. Res. **23**, 204 (2008).
100 K. R. Gadelrab, F. A. Bonilla, and M. Chiesa, Densification modeling of fused silica under nanoindentation, J. Non-Cryst. Solids **358**, 392 (2012).
101 X. Li, W. Zhang, M. Han, F. Xie, D. Li, J. Zhang, and B. Long, Indentation size effect: An improved mechanistic model incorporating surface undulation and indenter tip irregularity, J. Mater. Res. Tech. **23**, 143 (2023).
102 J. H. Gong, and M. Liu, A simple method for the determination of contact area for nanoindentation tests, Sci. Sin.-Phys. Mech. Astron. **53**, 214609 (2023).
103 M. Liu, Z. Cong, H. Fu, and P. Li, Relationships in instrumented indentation by Berkovich indenter, J. Mater. Res. **37**, 4084 (2022).
104 M. L. Oyen, Nanoindentation hardness of mineralized tissues, J. Biomech. **39**, 2699 (2006).
105 W. C. Oliver, and G. M. Pharr, An improved technique for determining hardness and elastic modulus using load and displacement sensing indentation experiments, J. Mater. Res. **7**, 1564 (1992).
106 C. Gao, and M. Liu, Instrumented indentation of fused silica by Berkovich indenter, J. Non-Cryst. Solids **475**, 151 (2017).
107 K. Zheng, C. Gao, F. He, Y. Lin, M. Liu, and J. Lin, Study on the interfacial functionary mechanism of rare-earth-solution-modified bamboo-fiber-reinforced resin matrix composites, Materials **11**, 1190 (2018).
108 C. Gao, and M. Liu, Power law creep of polycarbonate by Berkovich nanoindentation, Mater. Res. Express **4**, 105302 (2017).
109 C. Gao, L. Yao, and M. Liu, Berkovich nanoindentation of borosilicate K9 glass, Opt. Eng. **57**, 1 (2018).
110 J. Woirgard, J. C. Dargenton, C. Tromas, and V. Audurier, A new technology for nanohardness measurements: Principle and applications, Surf. Coat. Tech. **100-101**, 103 (1998).
111 Y. T. Cheng, and C. M. Cheng, Scaling, dimensional analysis, and indentation measurements, Mater. Sci. Eng.-R-Rep. **44**, 91 (2004).
112 J. Malzbender, G. de With, and J. den Toonder, The P-h^2 relationship in indentation, J. Mater. Res. **15**, 1209 (2000).
113 Y. T. Cheng, and C. M. Cheng, Relationships between hardness,

elastic modulus, and the work of indentation, Appl. Phys. Lett. **73**, 614 (1998).
114 Y. T. Cheng, Z. Li, and C. M. Cheng, Scaling relationships for indentation measurements, Philos. Mag. A **82**, 1821 (2002).
115 A. E. Giannakopoulos, and S. Suresh, Determination of elastoplastic properties by instrumented sharp indentation, Scripta Mater. **40**, 1191 (1999).
116 J. Malzbender, and G. de With, Indentation load-displacement curve, plastic deformation, and energy, J. Mater. Res. **17**, 502 (2002).
117 J. Chen, and S. J. Bull, Relation between the ratio of elastic work to the total work of indentation and the ratio of hardness to Young's modulus for a perfect conical tip, J. Mater. Res. **24**, 590 (2009).
118 M. Sakai, Simultaneous estimate of elastic/plastic parameters in depth-sensing indentation tests, Scripta Mater. **51**, 391 (2004).
119 J. Gong, H. Miao, and Z. Peng, Analysis of the nanoindentation data measured with a Berkovich indenter for brittle materials: Effect of the residual contact stress, Acta Mater. **52**, 785 (2004).
120 J. Gong, B. Deng, and D. Jiang, A universal function for the description of nanoindentation unloading data: Case study on soda-lime glass, J. Non-Cryst. Solids **544**, 120067 (2020).
121 S. A. Shahdad, J. F. McCabe, S. Bull, S. Rusby, and R. W. Wassell, Hardness measured with traditional Vickers and Martens hardness methods, Dent. Mater. **23**, 1079 (2007).
122 D. Ma, and C. W. Ong, Further analysis of energy-based indentation relationship among Young's modulus, nominal hardness, and indentation work, J. Mater. Res. **25**, 1131 (2010).
123 L. Chen, Q. Du, M. Yu, X. Guo, and W. Zhao, Measuring the effect of residual stress on the machined subsurface of Inconel 718 by nanoindentation, PLoS ONE **16**, e0245391 (2021).
124 M. Sakai, The Meyer hardness: A measure for plasticity? J. Mater. Res. **14**, 3630 (1999).
125 I. N. Sneddon, The relation between load and penetration in the axisymmetric boussinesq problem for a punch of arbitrary profile, Int. J. Eng. Sci. **3**, 47 (1965).
126 M. L. Oyen, and R. F. Cook, Load-displacement behavior during sharp indentation of viscous-elastic-plastic materials, J. Mater. Res. **18**, 139 (2003).
127 M. Asmani, C. Kermel, A. Leriche, and M. Ourak, Influence of porosity on Young's modulus and Poisson's ratio in alumina ceramics, J. Eur. Ceram. Soc. **21**, 1081 (2001).
128 G. R. Anstis, P. Chantikul, B. R. Lawn, and D. B. Marshall, A critical evaluation of indentation techniques for measuring fracture toughness: I, direct crack measurements, J. Am. Ceram. Soc. **64**, 533 (1981).
129 A. G. Evans, and E. A. Charles, Fracture toughness determinations by indentation, J. Am. Ceram. Soc. **59**, 371 (2006).
130 K. Sunil kumar, and D. Bishnoi, Pressure exertion and heat dissipation analysis on uncoated and ceramic (Al_2O_3, TiO_2 and ZrO_2) coated braking pads, Mater. Today-Proc. **74**, 774 (2022).
131 H. X. Geng, C. H. FU, X. L. Jiang, H. M. Xie, and C. Q. Chen, Measuring elastic modulus of ZrO_2 ceramics based on three-dimension digital image correlation, Exp. Technol. Manage. **32**, 60 (2015).
132 A. Pajares, F. Guiberteau, A. Dominguez-Rodriguez, and A. H. Heuer, Microhardness and fracture toughness anisotropy in cubic zirconium oxide single crystals, J. Am. Ceram. Soc. **71**, 332 (1988).
133 G. A. Gogotsi, B. A. Ozerskii, and O. B. Oksametnaya, Behavior of polycrystalline zirconium dioxide and single crystals during indentation, Refractories **33**, 453 (1992).
134 M. Liu, Z. Xu, and R. Fu, Micromechanical and microstructure characterization of BaO-Sm_2O_3–5TiO_2 ceramic with addition of Al_2O_3, Ceram. Int. **48**, 992 (2022).
135 J. S. Field, M. V. Swain, and R. D. Dukino, Determination of fracture toughness from the extra penetration produced by indentation-induced pop-in, J. Mater. Res. **18**, 1412 (2003).
136 D. G. Li, Y. C. Liang, and Q. S. Bai, Nano-indentation experiments on anisotropic mechanical properties of single crystal silicon, Aviat. Precis. Manuf. Technol. **44**, 9 (2008).
137 B. R. Lawn, A. G. Evans, and D. B. Marshall, Elastic/plastic indentation damage in ceramics: The median/radial crack system, J. Am. Ceram. Soc. **63**, 574 (1980).
138 K. Yasutake, M. Iwata, K. Yoshii, M. Umeno, and H. Kawabe, Crack healing and fracture strength of silicon crystals, J. Mater. Sci. **21**, 2185 (1986).
139 G. Farges, and D. Degout, Interpretation of the indentation size effect in vickers microhardness measurements-absolute hardness of materials, Thin Solid Films **181**, 365 (1989).
140 M. Liu, J. Wu, and C. Gao, Sliding of a diamond sphere on K9 glass under progressive load, J. Non-Cryst. Solids **526**, 119711 (2019).
141 V. Le Houérou, J. C. Sangleboeuf, S. Dériano, T. Rouxel, and G. Duisit, Surface damage of soda-lime-silica glasses: Indentation scratch behavior, J. Non-Cryst. Solids **316**, 54 (2003).
142 S. Bruns, L. Petho, C. Minnert, J. Michler, and K. Durst, Fracture toughness determination of fused silica by cube corner indentation cracking and pillar splitting, Mater. Des. **186**, 108311 (2020).
143 H. Xiao, R. Liang, O. Spires, H. Wang, H. Wu, and Y. Y. Zhang, Evaluation of surface and subsurface damages for diamond turning of ZnSe crystal, Opt. Express **27**, 28364 (2019).
144 H. Yagi, T. Yanagitani, T. Numazawa, and K. Ueda, The physical properties of transparent $Y_3Al_5O_{12}$, Ceram. Int. **33**, 711 (2007).
145 D. Du, Y. Wu, Y. Zhao, M. Lu, and H. Huang, Deformation and fracture behaviours of a YAG single crystal characterized using nanoindentation method, Mater. Charact. **164**, 110302 (2020).
146 L. Mezeix, and D. J. Green, Comparison of the mechanical properties of single crystal and polycrystalline yttrium aluminum garnet, Int. J. Appl. Ceram. Tech. **3**, 166 (2006).
147 T. Yanagida, M. Koshimizu, N. Kawano, G. Okada, and N. Kawaawaguchi, Optical and scintillation properties of $ScAlMgO_4$ crystal grown by the floating zone method, Mater. Res. Bull. **95**, 409 (2017).
148 T. Zhou, Y. Liang, W. Huang, N. Ye, and Y. Zou, Single-crystal Structure of $ScAlMgO_4$, Chin. J. Struct. Chem. **28**, 947 (2009).
149 Y. Wang, Y. Lian, Z. You, J. Li, Z. Zhu, G. Lakshminarayana, and C. Tu, Bulk crystal growth and mechanical and spectroscopic features comparison of Dy^{3+}-doped $(Lu_xY_{1-x})_3Al_5O_{12}$ (x = 0, 1/3, 1/2, 2/3) single crystals for yellow lasers, J. Lumin. **241**, 118452 (2022).
150 A. C. Fischer-Cripps, Nanoindentation (Springer Science+Business Media, New York, 2011).
151 K. Tao, V. A. Khonik, and J. C. Qiao, Indentation creep dynamics in metallic glasses under different structural states, Int. J. Mech. Sci. **240**, 107941 (2023).
152 X. Long, W. Tang, Y. Feng, C. Chang, L. M. Keer, and Y. Yao, Strain rate sensitivity of sintered silver nanoparticles using rate-jump indentation, Int. J. Mech. Sci. **140**, 60 (2018).
153 X. Long, Z. Shen, Q. Jia, J. Li, R. Dong, Y. Su, X. Yang, and K. Zhou, Determine the unique constitutive properties of elastoplastic materials from their plastic zone evolution under nanoindentation, Mech. Mater. **175**, 104485 (2022).
154 X. Long, Q. Jia, Z. Shen, M. Liu, and C. Guan, Strain rate shift for constitutive behaviour of sintered silver nanoparticles under nanoindentation, Mech. Mater. **158**, 103881 (2021).
155 J. Jang, and G. M. Pharr, Influence of indenter angle on cracking in Si and Ge during nanoindentation, Acta Mater. **56**, 4458 (2008).
156 T. An, L. L. Wang, H. W. Tian, M. Wen, and W. T. Zheng, Deformation and fracture of TiN coating on a Si(111) substrate during nanoindentation, Appl. Surf. Sci. **257**, 7475 (2011).
157 Y. W. Bao, W. Wang, and Y. C. Zhou, Investigation of the relationship between elastic modulus and hardness based on depth-sensing indentation measurements, Acta Mater. **52**, 5397 (2004).
158 J. Nohava, J. Čech, M. Havlíček, and R. Consiglio, Indenter wear study and proposal of a simple method for evaluation of indenter blunting, J. Mater. Res. **36**, 4449 (2021).
159 W. Huang, and J. Yan, Deformation behaviour of soft-brittle polycrystalline materials determined by nanoscratching with a sharp

indenter, Precision Eng. **72**, 717 (2021).
160 H. Xiao, S. Yin, C. F. Cheung, F. Zhang, H. Cao, and C. Wang, Material removal behavior analysis of ZnSe crystal during side-forward nanoscratching, Int. J. Mech. Sci. **241**, 107968 (2023).
161 C. Pu, L. Dai, H. Li, H. Hu, K. Liu, L. Yang, and M. Hong, Pressure-induced phase transitions of ZnSe under different pressure environments, AIP Adv. **9**, 025004 (2019).
162 I. Yonenaga, K. Watanabe, S. Itoh, and S. Fujiwara, Dynamics and characters of dislocations in ZnSe, J. Mater. Sci. **41**, 2601 (2006).
163 B. Huang, M. H. Zhao, and T. Y. Zhang, Indentation delamination and indentation fracture in ZnO/Si systems, MRS Proc. **687**, B5.14 (2001).
164 N. Kedir, D. C. Faucett, S. R. Choi, and N. P. Bansal, Slow-crack-growth and indentation damage in calcium magnesium aluminosilicate (CMAS) glass from desert sand, Ceram. Int. **44**, 2676 (2018).
165 H. S. Kim, and S. H. Park, Vickers crack extension and residual fracture strength of annealed and thermally tempered glass in water, J. Eur. Ceram. Soc. **42**, 1743 (2022).
166 S. E. Grillo, M. Ducarroir, M. Nadal, E. Tourni , and J. P. Faurie, Nanoindentation of Si, GaP, GaAs and ZnSe single crystals, J. Phys. D-Appl. Phys. **36**, L5 (2003).
167 G. M. Pharr, E. G. Herbert, and Y. Gao, The indentation size effect: A critical examination of experimental observations and mechanistic interpretations, Annu. Rev. Mater. Res. **40**, 271 (2010).
168 I. Manika, and J. Maniks, Size effects in micro- and nanoscale indentation, Acta Mater. **54**, 2049 (2006).
169 Y. M. Soifer, A. Verdyan, and L. Rapoport, Nanoindentation size effect in alkali-halide single crystals, Mater. Lett. **56**, 127 (2002).
170 J. Luo, H. Wang, C. Xi, H. Zhai, Y. Gu, and C. Zhang, Indentation size effect-crack propagation model and finite element simulation verification for microhardness test of ceramic materials, Ceram. Int. **47**, 4914 (2021).
171 T. T. Zhu, A. J. Bushby, and D. J. Dunstan, Size effect in the initiation of plasticity for ceramics in nanoindentation, J. Mech. Phys. Solids **56**, 1170 (2008).
172 O. Petruš, R. Sedlák, T. Csanádi, A. Naughton-Duszová, M. Vojtko, P. Hvizdoš, and J. Dusza, Indentation size effect in the hardness measurements of high entropy carbides, Ceram. Int. **49**, 24207 (2023).
173 P. Maiti, J. Ghosh, and A. K. Mukhopadhyay, New observations and critical assessments of incipient plasticity events and indentation size effect in nanoindentation of ceramic nanocomposites, Ceram. Int. **46**, 3144 (2020).
174 C. S. Han, Influence of the molecular structure on indentation size effect in polymers, Mater. Sci. Eng.-A **527**, 619 (2010).
175 S. S. Hirmukhe, A. Sharma, S. H. Nandam, H. Hahn, K. E. Prasad, and I. Singh, Investigation of softening induced indentation size effect in nanoglass and metallic glasss, J. Non-Cryst. Solids **577**, 121316 (2022).
176 Z. Shi, C. Wei, S. Zhang, W. Wang, H. Zhang, Y. Wu, and M. Ma, Nanoindentation study on room-temperature creep behavior of $Ir_{33}Ni_{28}Ta_{39}$ bulk metallic glass, J. Non-Cryst. Solids **603**, 122132 (2023).
177 D. Tang, L. Zhao, H. Wang, D. Li, Y. Peng, and P. Wu, The role of rough surface in the size-dependent behavior upon nano-indentation, Mech. Mater. **157**, 103836 (2021).
178 W. D. Nix, and H. Gao, Indentation size effects in crystalline materials: A law for strain gradient plasticity, J. Mech. Phys. Solids **46**, 411 (1998).
179 J. Cai, F. Li, T. Liu, and B. Chen, Microindentation study of Ti-6Al-4V alloy, Mater. Des. **32**, 2756 (2011).
180 C. Hays, and E. G. Kendall, An analysis of Knoop microhardness, Metallography **6**, 275 (1973).
181 S. J. Bull, T. F. Page, and E. H. Yoffe, An explanation of the indentation size effect in ceramics, Philos. Mag. Lett. **59**, 281 (1989).
182 H. Li, Y. H. Han, and R. C. Bradt, Knoop microhardness of single crystal sulphur, J. Mater. Sci. **29**, 5641 (1994).
183 J. Gong, J. Wu, and Z. Guan, Examination of the indentation size effect in low-load vickers hardness testing of ceramics, J. Eur. Ceram. Soc. **19**, 2625 (1999).
184 B. R. Lawn, and V. R. Howes, Elastic recovery at hardness indentations, J. Mater. Sci. **16**, 2745 (1981).
185 P. Maiti, M. Bhattacharya, P. S. Das, P. S. Devi, and A. K. Mukhokhopadhyay, Indentation size effect and energy balance issues in nanomechanical behavior of ZTA ceramics, Ceram. Int. **44**, 9753 (2018).
186 A. Bolshakov, and G. M. Pharr, Influences of pileup on the measurement of mechanical properties by load and depth sensing indentation techniques, J. Mater. Res. **13**, 1049 (1998).
187 D. Misra, S. M. Shariff, S. Mukhopadhyay, and S. Chatterjee, Analysis of instrumented scratch hardness and fracture toughness properties of laser surface alloyed tribological coatings, Ceram. Int. **44**, 4248 (2018).
188 M. J. M. Ridzuan, M. S. Abdul Majid, A. Khasri, E. H. D. Gan, Z. M. Razlan, and S. Syahrullail, Effect of pineapple leaf (PALF), napier, and hemp fibres as filler on the scratch resistance of epoxy composites, J. Mater. Res. Tech. **8**, 5384 (2019).
189 L. Riester, P. J. Blau, E. Lara-Curzio, and K. Breder, Nanoindentation with a Knoop indenter, Thin Solid Films **377-378**, 635 (2000).
190 G. BEN Ghorbal, A. Tricoteaux, A. Thuault, G. Louis, and D. Chicot, Mechanical characterization of brittle materials using instrumented indentation with Knoop indenter, Mech. Mater. **108**, 58 (2017).
191 T. Lube, Indentation crack profiles in silicon nitride, J. Eur. Ceram. Soc. **21**, 211 (2001).
192 J. H. Gong, and Z. D. Guan, Fracture from Knoop indentation-induced flaws in sintered silicon carbide and hot-pressed silicon Nitride, Key Eng. Mater. **224-226**, 765 (2002).
193 F. Rickhey, J. H. Lee, and H. Lee, XFEM investigation on Knoop indentation cracking: Fracture toughness and aspect-ratio of radial-median cracks, Mater. Des. **107**, 393 (2016).
194 E. Amitay-Sadovsky, and H. D. Wagner, Evaluation of Young's modulus of polymers from Knoop microindentation tests, Polymer **39**, 2387 (1998).
195 F. Delobel, S. Lemonnier, R. D'Elia, and J. Cambedouzou, Effects of density on the mechanical properties of spark plasma sintered β-SiC, Ceram. Int. **46**, 13244 (2020).
196 P. Intawin, S. Panyata, A. Kraipok, T. Tunkasiri, S. Eitssayeam, and K. Pengpat, Effects of TiO_2 content and thermal parameters on crystallization kinetics and mechanical properties of phosphate based glass system, Thermochim. Acta **690**, 178699 (2020).
197 P. V. Raja Shekar, D. Nagaraju, C. Sateesh Chandra, D. Madhavi Latha, and K. Kishan Rao, Investigations on surface and mechanical properties of bis-thiourea cadmium iodide—A non-linear optical crystal, Solid State Sci. **107**, 106353 (2020).
198 A. Darabi, and F. Azarmi, Investigation on relationship between microstructural characteristics and mechanical properties of wire-arc-sprayed Zn-Al coating, J. Therm. Spray Tech. **29**, 297 (2020).
199 D. B. Marshall, T. Noma, and A. G. Evans, A simple method for determining elastic-modulus-to-hardness ratios using Knoop indentation measurements, J. Am. Ceram. Soc. **65**, 175 (1982).
200 J. Conway, Determination of hardness to elastic modulus ratios using Knoop indentation measurements and a model based on loading and reloading half-cycles, J. Mater. Sci. **21**, 2525 (1986).
201 G. Ben Ghorbal, A. Tricoteaux, A. Thuault, G. Louis, and D. Chi-Chicot, Comparison of conventional Knoop and Vickers hardness of ceramic materials, J. Eur. Ceram. Soc. **37**, 2531 (2017).
202 M. Liu, Q. Zheng, and C. Gao, Characterization of mechanical properties of bulk metallic glasses based on Knoop hardness, Chin. J. Solid Mech. **42**, 376 (2021).
203 M. Liu, and S. Chen, Micromechanical characterization of zirconia and silicon nitride ceramics using indentation and scratch methods, Ceram. Int. **50**, 19982 (2024).
204 H. C. Hyun, F. Rickhey, J. H. Lee, J. H. Hahn, and H. Lee, Characteristics of indentation cracking using cohesive zone finite

element techniques for pyramidal indenters, Int. J. Solids Struct. **51**, 4327 (2014).
205 M. Liu, Q. Zheng, and C. Gao, Sliding of a diamond sphere on fused silica under ramping load, Mater. Today Commun. **25**, 101684 (2020).
206 L. Zhang, and L. Wang, Optimization of site investigation program for reliability assessment of undrained slope using Spearman rank correlation coefficient, Comput. Geotech. **155**, 105208 (2023).
207 M. Liu, D. Hou, Y. Wang, and G. Lakshminarayana, Micromechanical properties of Dy^{3+} ion-doped $(Lu_xY_{1-x})_3Al_5O_{12}$ (x = 0, 1/3, 1/2) single crystals by indentation and scratch tests, Ceram. Int. **49**, 4482 (2022).
208 X. Jiang, J. Zhao, and X. Jiang, Correlation between hardness and elastic moduli of the covalent crystals, Comput. Mater. Sci. **50**, 2287 (2011).
209 H. Y. Chung, M. B. Weinberger, J. M. Yang, S. H. Tolbert, and R. B. Kaner, Correlation between hardness and elastic moduli of the ultraincompressible transition metal diborides RuB_2, OsB_2, and ReB_2, Appl. Phys. Lett. **92**, 261904 (2008).

利用仪器化压入表征脆性固体的弹性模量和硬度

徐智通, 刘明, 龚江宏

摘要 利用纳米压入测试了各种脆性固体(比如: 陶瓷、半导体、玻璃、单晶和激光材料)的缩减弹性模量E_r和压入硬度H_{IT}, 比较了各种分析方法: 一些方法需要压头的面积函数, 比如Oliver & Pharr(OP)方法和基于名义硬度的方法; 另外一些方法不需要校准压头, 比如基于能量、位移、接触深度和接触硬度的方法. 努氏压头下压痕的弹性恢复也被用于评估脆性固体材料的弹性模量. 对于脆性固体, H_{IT}/E_r与纳米压入无量纲特征量(如弹性功与总功之比、残余位移与最大位移之比)之间的关系是非线性的, 而不是线性的. 对于脆性固体(传统玻璃除外), 根据E_r计算的塑性硬度H_p与$E_r\sqrt{H_{IT}}$成正比.